Astronomy & Astrophysics

A matched filter approach for blind joint detection of galaxy clusters in X-ray and SZ surveys

P. Tarrío[1,2], J.-B. Melin[1], and M. Arnaud[1,2]

[1] IRFU, CEA, Université Paris-Saclay, 91191 Gif-sur-Yvette, France
e-mail: paula.tarrio-alonso@cea.fr
[2] Université Paris Diderot, AIM, Sorbonne Paris Cité, CEA, CNRS, 91191 Gif-sur-Yvette, France

ABSTRACT

The combination of X-ray and Sunyaev–Zeldovich (SZ) observations can potentially improve the cluster detection efficiency, when compared to using only one of these probes, since both probe the same medium, the hot ionized gas of the intra-cluster medium. We present a method based on matched multifrequency filters (MMF) for detecting galaxy clusters from SZ and X-ray surveys. This method builds on a previously proposed joint X-ray–SZ extraction method and allows the blind detection of clusters, that is finding new clusters without knowing their position, size, or redshift, by searching on SZ and X-ray maps simultaneously. The proposed method is tested using data from the ROSAT all-sky survey and from the *Planck* survey. The evaluation is done by comparison with existing cluster catalogues in the area of the sky covered by the deep SPT survey. Thanks to the addition of the X-ray information, the joint detection method is able to achieve simultaneously better purity, better detection efficiency, and better position accuracy than its predecessor *Planck* MMF, which is based on SZ maps alone. For a purity of 85%, the X-ray–SZ method detects 141 confirmed clusters in the SPT region; to detect the same number of confirmed clusters with *Planck* MMF, we would need to decrease its purity to 70%. We provide a catalogue of 225 sources selected by the proposed method in the SPT footprint, with masses ranging between 0.7 and $14.5 \times 10^{14} \, M_\odot$ and redshifts between 0.01 and 1.2.

Key words. methods: data analysis – techniques: image processing – galaxies: clusters: general – large-scale structure of Universe – X-rays: galaxies: clusters

1. Introduction

Galaxy clusters can be detected from observations at different bands of the electromagnetic spectrum, each of them probing a different component of the cluster. In optical observations we can see the individual galaxies inside the cluster, which contribute to around 1% of the total cluster mass. Clusters are identified in these images as overdensities of galaxies. Clusters can also be detected in X-ray observations where they appear as bright sources with extended emission. In these images we observe the emission of the hot gas of the intracluster medium (ICM), which accounts for 10–15% of the cluster mass. Over the last decade, this gas has also begun to be detected thanks to the characteristic spectral distortion it produces on the cosmic microwave background (CMB) due to Compton scattering of the CMB photons by the ICM electrons. This effect is known as the Sunyaev–Zeldovich (SZ) effect (Sunyaev & Zeldovich 1970, 1972).

State-of-the-art galaxy cluster detection techniques usually rely on the analysis of single-survey observations. However, combining information from different surveys at different wavelengths can potentially improve the detection performance, allowing us to find more distant or less massive clusters. Although multiwavelength, multisurvey detection of clusters was theoretically conceived some years ago (Maturi 2007; Pace et al. 2008), it is a very complex task and, to date, has only been attempted in practice in the pilot study of Schuecker et al. (2004) on X-ray data from the ROSAT All-Sky Survey (RASS; Truemper 1993; Voges et al. 1999) and optical data from the

Sloan Digital Sky Survey (SDSS; York et al. 2000). In our previous work (Tarrío et al. 2016), we proposed a new analysis tool based on matched multifrequency filters (MMF) for extracting clusters from SZ and X-ray maps. The method was based on the combination of the classical SZ MMF (Herranz et al. 2002; Melin et al. 2006, 2012) and an analogous single-frequency matched filter developed for X-ray maps. It was shown that combining these two complementary sources of information improved the signal-to-noise ratio (S/N) with respect to SZ-only or X-ray-only cluster extraction, and also provided correct photometry as long as the physical relation between X-ray and SZ emission of the clusters, namely the expected F_X/Y_{500} relation, was known. The filter was used as an extraction tool to estimate some properties of already detected clusters, but not to detect new clusters in a blind manner, since the position, the size, and the redshift of the clusters were assumed to be known.

In this paper we propose a blind detection method based on the X-ray–SZ filter studied in Tarrío et al. (2016). The goal is to adapt this filter to use it as a blind cluster detection tool, given that we do not know the position, the size, and the redshift of the clusters. As demonstrated in Tarrío et al. (2016), combining X-ray and SZ information increases the cluster S/N with respect to single-map extractions. This gain in S/N will translate directly into a higher detection probability for a given threshold in the S/N. We would also expect to obtain, in principle, a higher purity than when using the classical SZ MMF since the combined version will clean out objects whose emission is far from the expected F_X/Y_{500} relation. However, even

if an object does not follow the expected relation, it could still pass the detection threshold if it has a very strong signal in the X-ray band. This is similar to the strong infrared emissions that were detected with the classical SZ MMF used by the Planck Collaboration VIII (2011); Planck Collaboration XXIX (2014); Planck Collaboration XXVII (2016) even though their spectra did not fit the expected SZ spectrum. This may be the case of some non-cluster X-ray sources, such as active galactic nuclei (AGNs). Since the X-ray filter was designed to be easily compatible with the classical SZ MMF and it is not specifically optimized for X-ray cluster detection, it does not consider the extent of the sources, as other X-ray cluster detection techniques do (Böhringer et al. 2000; Vikhlinin et al. 1998; Pacaud et al. 2006; Ebeling & Wiedenmann 1993; Scharf et al. 1997). As a result, when we add the X-ray information, we will also add false detections produced by non-cluster X-ray sources (mainly AGNs). Therefore, as already noted in Tarrío et al. (2016), the main challenge to be solved when using the proposed X-ray–SZ MMF for blind detection is to obtain a high purity.

The proposed method is applied to observations from the ROSAT All-Sky Survey (RASS) and the *Planck* survey, the latest full-sky X-ray and SZ surveys available to date. Nevertheless, the proposed joint detection technique is general and also applicable to other surveys, including those from future missions such as e-ROSITA (Merloni et al. 2012), a four-year X-ray survey which is planned to start in 2018 and which will be much deeper than RASS.

The structure of the paper is as follows. Section 2 presents RASS and *Planck* observations. In Sect. 3 we describe the joint X-ray–SZ detection algorithm. Section 4 presents an evaluation of its performance using RASS and *Planck* maps by comparing its results with other cluster catalogues in the SPT region. Finally, we conclude the paper and discuss ongoing and future research directions in Sect. 5.

Throughout, we adopt a flat ΛCDM cosmological model with $H_0 = 70 \, \mathrm{km \, s^{-1} \, Mpc^{-1}}$ and $\Omega_M = 1 - \Omega_\Lambda = 0.3$. We define R_{500} as the radius within which the average density of the cluster is 500 times the critical density of the universe, θ_{500} as the corresponding angular radius, and M_{500} as the mass enclosed within R_{500}.

2. Description of the observations

Although the joint algorithm proposed in this paper is a general technique that can be applied, in principle, to any X-ray and SZ surveys of the sky, we have tested it in this paper using all-sky maps from the *Planck* and RASS surveys. In this section, we briefly describe these observations.

2.1. RASS data description

The ROSAT All-Sky Survey (RASS) is, to date, the only full-sky X-ray survey conducted with an X-ray telescope (Truemper 1993; Voges et al. 1999). The survey data release[1] contains 1378 individual RASS fields in three different bands: TOTAL (0.1–2.4 keV), HARD (0.5–2.0 keV), and SOFT (0.1–0.4 keV). Each field covers an area of $6.4 \, \mathrm{deg} \times 6.4 \, \mathrm{deg}$ (512×512 pixels) and has a resolution of 0.75 arcmin/pixel.

In this paper, we use an X-ray all-sky HEALPix map that we built from the HARD band information. This map has a

---

[1] ftp://legacy.gsfc.nasa.gov/rosat/data/pspc/processed_data/rass/release, or http://www.xray.mpe.mpg.de/rosat/survey/rass-3/main/help.html#ftp

resolution of 0.86 arcmin/pixel (HEALPix resolution closest to the RASS resolution). The details of its construction can be found in Appendix B of Tarrío et al. (2016). Although our approach could optimally include all X-ray bands, we chose to use only the HARD band. This provides a better S/N for the clusters because the SOFT band is dominated by the diffuse X-ray background of the local bubble. This is a common choice in cluster detection surveys based on RASS data, such as REFLEX (Böhringer et al. 2001, 2013).

2.2. Planck data description

Planck is the most recent space mission that was launched to measure the anisotropy of the CMB. It observed the sky in nine frequency bands from 30 to 857 GHz with high sensitivity and angular resolution. The Low Frequency Instrument (LFI) covers the 30, 44, and 70 GHz bands, while the High Frequency Instrument (HFI) covers the 100, 143, 217, 353, 545, and 857 GHz bands.

In this paper, we use only the six temperature channel maps of HFI, which are the same channels used by the *Planck* Collaboration to produce their cluster catalogues (Planck Collaboration VIII 2011; Planck Collaboration XXIX 2014; Planck Collaboration XXVII 2016). In particular, we used the latest version of these maps; their description can be found in Planck Collaboration VIII (2016). The published full resolution maps have a resolution of 1.72 arcmin/pixel. However, to make them directly compatible with the all-sky X-ray map mentioned above, we up-sampled them to a resolution of 0.86 arcmin/pixel by zero-padding in the spherical harmonics domain.

3. Joint detection of galaxy clusters on X-ray and SZ maps

In this section, we describe the proposed algorithm for the blind detection of galaxy clusters using X-ray and sub-mm maps. The algorithm is based on the X-ray–SZ extraction method proposed in Tarrío et al. (2016), which extracts the characteristics of a cluster given its known position, size, and redshift. In this paper, we adapted this extraction method to perform a blind detection of clusters, i.e. to discover clusters in the maps without knowing their positions, sizes, or redshifts.

3.1. X-ray–SZ MMF

Let us first briefly recall the joint X-ray–SZ extraction method proposed in Tarío et al. (2016). This method is based on a matched filter approach and was designed to be compatible with the SZ MMF known as MMF3, described by Melin et al. (2012) and used by the Planck Collaboration VIII (2011); Planck Collaboration XXIX (2014); Planck Collaboration XXVII (2016) to construct their SZ cluster catalogues.

The main idea of the joint extraction algorithm is to consider the X-ray map as an additional SZ map at a given frequency and to introduce it, together with the other SZ maps, in the classical SZ-MMF. In order to do so, the X-ray map needs to be converted into an equivalent SZ map at a reference frequency ν_{ref}, leveraging the expected F_X/Y_{500} relation. The details of this conversion are described in Appendix B of Tarrío et al. (2016). Once the X-ray map is expressed in the same units as the SZ maps, we can apply the classical MMF to the complete set of maps (the original N_ν SZ maps obtained at sub-mm frequencies $\nu_1, \ldots, \nu_{N_\nu}$, and an additional SZ map at the reference frequency ν_{ref} obtained

from the X-ray map). The reference frequency ν_{ref} is just a fiducial value with no effect on the extraction algorithm. In our case, we took $\nu_{ref} = 1000$ GHz.

The X-ray–SZ MMF presented in Tarrío et al. (2016) is given, in Fourier space[2], by

$$\boldsymbol{\Psi}_{\theta_s}(\mathbf{k}) = \sigma_{\theta_s}^2 \mathbf{P}^{-1}(\mathbf{k}) \mathbf{F}_{\theta_s}(\mathbf{k}) \tag{1}$$

with

$$\sigma_{\theta_s}^2 = \left[\sum_{\mathbf{k}} \mathbf{F}_{\theta_s}^T(\mathbf{k}) \mathbf{P}^{-1}(\mathbf{k}) \mathbf{F}_{\theta_s}(\mathbf{k}) \right]^{-1}, \tag{2}$$

where $\boldsymbol{\Psi}_{\theta_s}$ is a $(N_\nu + 1) \times 1$ column vector whose ith component will filter the map at observation frequency ν_i; $\sigma_{\theta_s}^2$ is, approximately, the background noise variance after filtering; and $\mathbf{P}(\mathbf{k})$ is the noise power spectrum, a $(N_\nu + 1) \times (N_\nu + 1)$ matrix whose ij component is given by $\left\langle N_i(\mathbf{k}) N_j^*(\mathbf{k}') \right\rangle = P_{ij}(\mathbf{k}) \delta(\mathbf{k} - \mathbf{k}')$, where $N_i(\mathbf{k})$ is the noise map at observation frequency ν_i, which includes instrumental noise and astrophysical sources different from the cluster signal (extragalactic point sources, diffuse Galactic emission, and the primary CMB anisotropy for the SZ maps and X-ray background for the X-ray map). We note that the properties of the noise are not the same in different sky regions; therefore, $\mathbf{P}(\mathbf{k})$ has to be calculated locally at each position. Finally, $\mathbf{F}_{\theta_s}$ is a $(N_\nu + 1) \times 1$ column vector defined as

$$\mathbf{F}_{\theta_s}(\mathbf{x}) = [j(\nu_1) T_1(\mathbf{x}), \ldots, j(\nu_{N_\nu}) T_{N_\nu}(\mathbf{x}), C j(\nu_{ref}) T_{\theta_s}^x(\mathbf{x})]^T, \tag{3}$$

where $j(\nu_i)$ is the SZ spectral function at frequency ν_i and $T_i(\mathbf{x}) = \tilde{T}_{\theta_s}(\mathbf{x}) * B_{\nu_i}(\mathbf{x})$ and $T_{\theta_s}^x(\mathbf{x}) = \tilde{T}_{\theta_s}^x(\mathbf{x}) * B_{xray}(\mathbf{x})$ are the convolutions of the cluster 2D spatial profiles ($\tilde{T}_{\theta_s}(\mathbf{x})$ for the SZ profile and $\tilde{T}_{\theta_s}^x(\mathbf{x})$ for the X-ray profile) with the point spread function (PSF) of the instruments at the different frequencies. The 2D cluster profiles $\tilde{T}_{\theta_s}(\mathbf{x})$ and $\tilde{T}_{\theta_s}^x(\mathbf{x})$ are normalized so that their central value is 1. Finally, the constant C is a geometrical factor that accounts for the different shapes of the SZ and X-ray 3D profiles; it is defined in Eq. (25) of Tarrío et al. (2016) as the ratio of the integrated fluxes of the normalized SZ and X-ray 3D profiles up to R_{500}. As we can see, the filter is determined by the shape of the cluster signal and by the power spectrum of the noise, hence the name of matched filter.

This matched filter approach relies on the knowledge of the normalized cluster profile. This profile is not known in practice, so we need to approximate it by the theoretical profile that best represents the clusters we want to detect. As in Tarrío et al. (2016), we assume the generalized Navarro–Frenk–White (GNFW) profile (Nagai et al. 2007) given by

$$p(x) \propto \frac{1}{(c_{500} x)^\gamma [1 + (c_{500} x)^\alpha]^{(\beta - \gamma)/\alpha}} \tag{4}$$

with parameters given by

$$[\alpha, \beta, \gamma, c_{500}] = [1.0510, 5.4905, 0.3081, 1.177] \tag{5}$$

and

$$[\alpha, \beta, \gamma, c_{500}] = [2.0, 4.608, 1.05, 1/0.303] \tag{6}$$

for the components corresponding to the original SZ maps and the additional X-ray map, respectively. These parameters come from assuming the 3D pressure profile of Arnaud et al. (2010) and the average gas density profile from Piffaretti et al. (2011), respectively. We note that $x = \theta/\theta_{500}$ represents here the 3D distance to the centre of the cluster in θ_{500} units, and θ_{500} relates to the characteristic cluster scale θ_s through the concentration parameter c_{500} ($\theta_s = \theta_{500}/c_{500}$). The cluster profile is then obtained by numerically integrating these 3D GNFW profiles along the line of sight.

Finally, this cluster profile needs to be convolved by the instrument beams. As in Tarrío et al. (2016), in this paper we use the six highest frequency *Planck* maps and the X-ray maps of the ROSAT All-Sky Survey. Therefore, we use the same instrument beams as in Tarrío et al. (2016), namely, a Gaussian PSF for the SZ components, with FWHM depending on the frequency, as shown in Table 6 of Planck Collaboration VIII (2016), and a PSF for the X-ray component that was estimated numerically by stacking observations of X-ray point sources from the Bright Source Catalogue (Voges et al. 1999).

Figure 1 shows two examples of the radial profiles of the filter $\boldsymbol{\Psi}_{\theta_s}$ for $\theta_s = 1$ and $\theta_s = 30$ arcmin where we can see the spectral and the spatial weighting introduced by the filter. The filter was computed at a random position, with galactic coordinates $260.356°$, $-20.332°$. We note that the last component of the filter corresponds to the X-ray band, and that its relative amplitude depends on the chosen reference frequency ν_{ref}.

3.2. Blind procedure

In Tarrío et al. (2016), the filter described above was proposed as an extraction tool, to estimate the flux of a cluster once we know that there is a cluster at a given position $\mathbf{x}_0$, and if we know its size θ_s and redshift (necessary to convert the X-ray into an equivalent SZ map through the F_X/Y_{500} relation). In this section we describe how this method is adapted to become a detection tool.
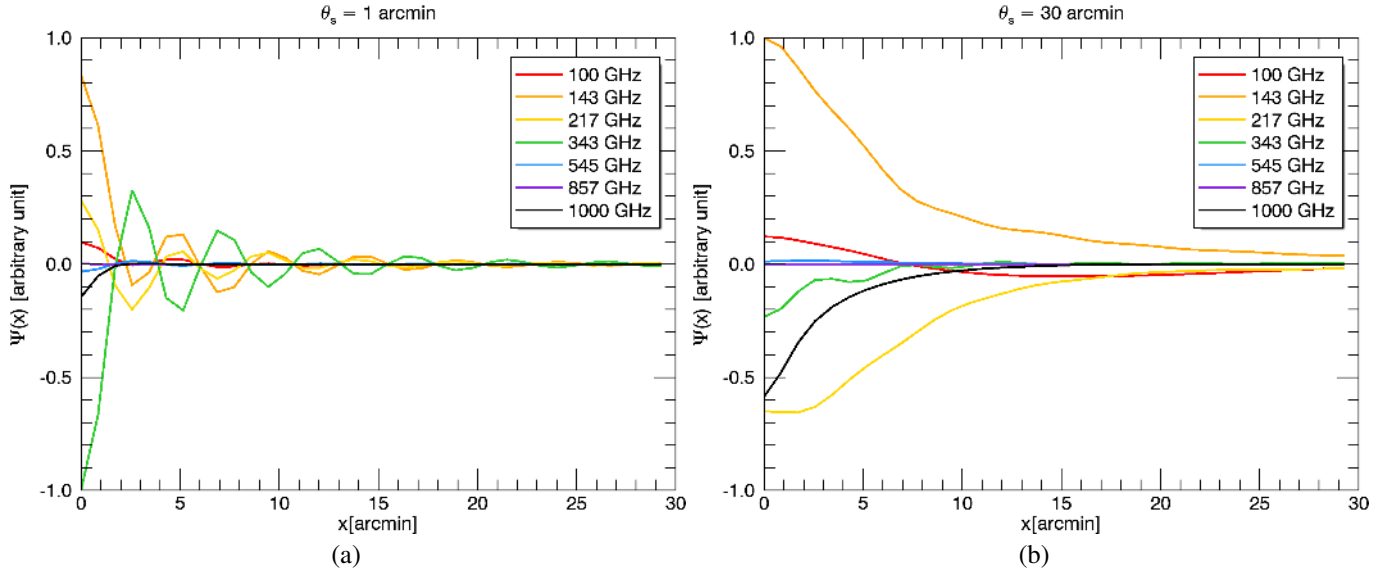
Given a set of $N_\nu + 1$ maps (SZ + X-ray) of a given region of the sky $\mathbf{M}(\mathbf{x}) = [M_1(\mathbf{x}), \ldots, M_{N_\nu}(\mathbf{x}), M_{ref}(\mathbf{x})]^T$, where M_{ref} is the X-ray map already converted into SZ units, the first step to detect new clusters consists of filtering the maps with the filter defined in Eq. (1) as

$$\hat{y}(\mathbf{x}) = \sum_{\mathbf{x}'} \boldsymbol{\Psi}_{\theta_s}^T(\mathbf{x}' - \mathbf{x}) \mathbf{M}(\mathbf{x}'). \tag{7}$$

In this way, we obtain a $\hat{y}$-map (filtered map) and a S/N map ($\hat{y}(\mathbf{x})/\sigma_{\theta_s}$) with the same size as the observed maps.

We note that to calculate the filter $\boldsymbol{\Psi}_{\theta_s}$, we first need to estimate the noise power spectrum $\mathbf{P}(\mathbf{k})$. This is done in practice from the X-ray and SZ images themselves, assuming that they contain mostly noise. In the case of the X-ray images, this assumption may not be true due to bright X-ray sources with strong signals. Therefore, to minimize this effect, we masked some regions of the X-ray images for the calculation of $\mathbf{P}(\mathbf{k})$. In particular, we masked the areas defined in Table 1 of Böhringer et al. (2001) corresponding to the Large and Small Magellanic Clouds, and we also masked the X-ray sources of the ROSAT bright source catalogue (Voges et al. 1999) that have a count rate >0.3 counts/s.

Since the size of the clusters is unknown, we repeat the filtering process using a set of N_s filters with different sizes, covering the expected range of radii. In our case, we vary θ_{500} from 0.94 to 35.31 arcmin, in $N_s = 32$ steps equally spaced in logarithmic

---

2 We use $\mathbf{k}$ to denote the 2D spatial frequency, corresponding to the 2D position $\mathbf{x}$ in the Fourier space. All the variables expressed as a function of $\mathbf{k}$ are thus to be understood as variables in the Fourier space.

Fig. 1. Examples of the matched filter $\boldsymbol{\Psi}_{\theta_s}$ for $\theta_s = 1$ arcmin (a) and $\theta_s = 30$ arcmin (b). The curves give the radial profiles of the filters, which are symmetric because we have chosen a symmetric cluster template. The filter is normalized so that its maximum amplitude is equal to 1.

scale. For each size, we obtain a filtered map and a S/N map. The clusters are then detected as peaks in these S/N maps, down to a given threshold.

Finally, for the conversion of the X-ray map into an equivalent SZ map we need to assume a F_X / Y_{500} relation, which depends on the redshift. As studied in Tarrío et al. (2016), the assumed F_X / Y_{500} relation does not have a big impact on the estimated S/N, which makes the detection robust against possible errors in the assumed relation. For this reason, we have fixed the redshift to a reference value of $z_{ref} = 0.8$ and assumed the relation found by the Planck Collaboration I (2012):

$$\frac{F_X \left[\text{erg s}^{-1} \text{ cm}^{-2} \right]}{Y_{500} \left[\text{arcmin}^2 \right]} = 4.95 \times 10^{-9} \cdot E(z)^{5/3} (1+z)^{-4} K(z), \qquad (8)$$

where the K-correction can be obtained by interpolating in Table 2 of Tarrío et al. (2016).

To implement the detection procedure in practice, we proceed in two phases.

1. Producing a preliminary list of candidates. In this first phase, we project the all-sky maps into 504 small $10° \times 10°$ tangential patches, as was done in MMF3 (Planck Collaboration VIII 2011; Planck Collaboration XXIX 2014; Planck Collaboration XXVII 2016). Each patch is filtered by the X-ray–SZ filter $\boldsymbol{\Psi}_{\theta_s}$ (Eq. (1)) using $N_s = 32$ different sizes, which produces N_s S/N maps. Then, we construct a list with the peaks in these maps that are above a specified S/N threshold q. The procedure is as follows:

   (a) We look for the highest peak among all the N_s S/N maps;
   (b) If it is above the specified threshold q, we include its position in a preliminary candidate list and mask it in the N_s S/N maps. The size of the mask is defined as the radius at which the value of the filtered template is 1% of its maximum value. The filtered template is the 2D cluster profile corresponding to the size at which the highest peak was found, convolved by the PSF, and filtered by the X-ray–SZ filter $\boldsymbol{\Psi}_{\theta_s}$ with the $N_s = 32$ different sizes. Thus, the size of the mask is different in each of the N_s S/N maps;

   (c) Then we repeat the search until there are no more peaks above the specified threshold.

   Finally, we merge the 504 lists into a single preliminary all-sky list of candidates by merging peaks that are close to each other by <10 arcmin, as was done in MMF3 (Planck Collaboration VIII 2011; Planck Collaboration XXIX 2014; Planck Collaboration XXVII 2016).

2. Refining the list of candidates. In this second phase, we reanalyse each candidate in the preliminary candidate list. This second phase is necessary to better estimate the candidate properties and S/N, since the results from the first phase may not be accurate. This is especially true if the candidate is situated close to a border of the map, since the estimated noise in this case may not be representative of the noise around the candidate. For each candidate we use the following procedure:

   (a) We produce a set of $N_\nu + 1$ (SZ + X-ray) $10° \times 10°$ tangential maps centred at the candidate position;
   (b) We filter these maps with the different filter sizes, obtaining N_s S/N maps;
   (c) We estimate the S/N of the detection by selecting a small circular region around the centre in each of the N_s S/N maps and by searching for local maxima inside this volume. This is necessary because the position of the peak may have changed slightly when centring the tangential maps. Among all the local maxima, we select the one with highest S/N that is not on the border of the circles (to avoid tails of nearby objects);
   (d) If this S/N is above a specified threshold q, we add the detection, with its new position and corresponding size, to the final candidate list, otherwise we discard it.

3.3. Determination of the threshold on the joint S/N

An important point of the blind joint detection algorithm is the selection of the threshold q that is applied to the peaks found in the first and second phases. The goal of this threshold is to discard false detections (noise peaks) with a given confidence. This can be achieved by setting the probability that a detection is due to a random fluctuation to a sufficiently low value. In the

Table 1. Average standard deviation of the X-ray filtered map $\sigma_{\theta_s}^x$ (in $\Delta T/T$ units) for different values of mean Poisson noise λ (in counts/pixel) and several filter sizes (in arcmin), corresponding to a map with exposure time of 400 s and $N_H = 2 \times 10^{20}$ cm^{-2}.

	$\lambda = 0.03$	$\lambda = 0.06$	$\lambda = 0.09$	$\lambda = 0.15$	$\lambda = 0.25$	$\lambda = 0.40$	$\lambda = 0.70$	$\lambda = 2.00$	$\lambda = 7.50$
$\theta_s = 0.80$	5.00e−5	7.08e−5	8.68e−5	1.12e−4	1.45e−4	1.84e−4	2.43e−4	4.10e−4	7.93e−4
$\theta_s = 1.28$	3.07e−5	4.34e−5	5.33e−5	6.90e−5	8.93e−5	1.13e−4	1.49e−4	2.52e−4	4.87e−4
$\theta_s = 2.04$	1.76e−5	2.49e−5	3.06e−5	3.96e−5	5.12e−5	6.49e−5	8.56e−5	1.44e−4	2.79e−4
$\theta_s = 3.25$	9.40e−6	1.33e−5	1.64e−5	2.12e−5	2.75e−5	3.48e−5	4.59e−5	7.73e−5	1.49e−4
$\theta_s = 5.19$	4.96e−6	7.03e−6	8.64e−6	1.12e−5	1.45e−5	1.84e−5	2.42e−5	4.08e−5	7.88e−5
$\theta_s = 8.29$	2.71e−6	3.86e−6	4.75e−6	6.17e−6	8.01e−6	1.01e−5	1.33e−5	2.24e−5	4.32e−5
$\theta_s = 13.23$	1.50e−6	2.14e−6	2.64e−6	3.44e−6	4.47e−6	5.67e−6	7.41e−6	1.24e−5	2.39e−5
$\theta_s = 21.12$	8.81e−7	1.26e−6	1.56e−6	2.04e−6	2.67e−6	3.38e−6	4.38e−6	7.29e−6	1.41e−5
$\theta_s = 30.00$	5.91e−7	8.51e−7	1.06e−6	1.39e−6	1.82e−6	2.30e−6	2.96e−6	4.90e−6	9.43e−6

Table 2. Average standard deviation of the SZ filtered maps $\sigma_{\theta_s}^{sz}$ (in $\Delta T/T$ units) for different values of mean Gaussian noise σ_{217} (in $\Delta T/T$ units) and several filter sizes (in arcmin).

	$\sigma_{217} = 10^{-5}$	$\sigma_{217} = 2 \times 10^{-5}$	$\sigma_{217} = 2.5 \times 10^{-5}$	$\sigma_{217} = 3 \times 10^{-5}$	$\sigma_{217} = 4 \times 10^{-5}$	$\sigma_{217} = 5 \times 10^{-5}$	$\sigma_{217} = 6 \times 10^{-5}$
$\theta_s = 0.80$	4.77e−5	9.01e−5	1.11e−4	1.33e−4	1.76e−4	2.18e−4	2.61e−4
$\theta_s = 1.28$	2.95e−5	5.56e−5	6.87e−5	8.19e−5	1.08e−4	1.35e−4	1.61e−4
$\theta_s = 2.04$	1.74e−5	3.25e−5	4.02e−5	4.79e−5	6.32e−5	7.86e−5	9.39e−5
$\theta_s = 3.25$	9.78e−6	1.82e−5	2.24e−5	2.67e−5	3.52e−5	4.37e−5	5.22e−5
$\theta_s = 5.19$	5.50e−6	1.01e−5	1.25e−5	1.48e−5	1.95e−5	2.43e−5	2.90e−5
$\theta_s = 8.29$	3.26e−6	5.94e−6	7.30e−6	8.68e−6	1.14e−5	1.42e−5	1.70e−5
$\theta_s = 13.23$	1.94e−6	3.50e−6	4.30e−6	5.11e−6	6.74e−6	8.37e−6	1.00e−5
$\theta_s = 21.12$	1.20e−6	2.16e−6	2.65e−6	3.15e−6	4.15e−6	5.16e−6	6.17e−6
$\theta_s = 30.00$	8.19e−7	1.48e−6	1.81e−6	2.15e−6	2.84e−6	3.53e−6	4.22e−6

MMF3 method, a fixed threshold is used under the assumption that the noise distribution is Gaussian, so that a fixed S/N threshold leads to a fixed number of noise peak detections. In the joint X-ray–SZ detection, the Gaussian assumption is no longer valid, as explained below, so the threshold must be selected differently.

The probability density function (PDF) of the S/N in the joint filtered maps depends on the noise properties of the observed maps. Due to the Poisson nature of the noise in the X-ray maps, the final PDF of the joint S/N is not Gaussian. Its shape depends on the exposure time of the X-ray map and also on the filter size. In particular, it becomes more long-tailed when the exposure time is low, especially for small filter sizes; in these cases, most of the pixels of the X-ray map contain zero photons, and just a few pixels contain one photon. As a consequence, the average background is very low and the S/N of the filtered map, defined as $\hat{y}(\mathbf{x})/\sigma_{\theta_s}$, at the few pixels with one photon can be easily quite high.

Since the PDF of the joint S/N will have different shapes in different regions of the sky, using a fixed S/N threshold to detect cluster candidates everywhere in the sky will produce a different number of false detections, e.g. more detections will appear in low exposure time regions due to single noise pixels with high S/N. To have an approximately constant number of false detections over the whole sky, we need to establish an adaptive threshold that depends on the noise characteristics of each region. Since the PDF of the joint S/N cannot be calculated analytically, we have determined this adaptive threshold numerically by means of Monte Carlo simulations.

In particular, we performed an experiment in which we simulated a set of $N_\nu + 1 = 7$ maps emulating in a simple manner the noise properties of *Planck* and RASS maps.

– The RASS noise map was simulated as a homogeneous Poisson random field, characterized by a given mean value λ (in counts/pixel). This noise represents the instrumental noise and the astrophysical X-ray background (mainly due to diffuse galactic emission and non-resolved point sources). To express this map into X-ray flux units, we assumed an exposure time of 400 s and a N_H of 2×10^{20} cm^{-2} (average values in the SPT region). We note that the simulation results obtained for these values can be converted to results that would be obtained for any other values of exposure time and N_H, as explained in Appendix A, so this choice does not have any implications. Finally, as was done with the real RASS maps, this X-ray flux map is converted into an equivalent SZ map at the reference frequency ν_{ref} by following the procedure detailed in Appendix B of Tarrío et al. (2016).

– The $N_\nu = 6$ *Planck* noise maps were simulated as the sum of two independent components: primary anisotropies and white Gaussian noise. First, we used the *Planck* Sky Model (Delabrouille et al. 2013) to obtain a realization of the CMB for the $N_\nu = 6$ *Planck* frequencies (100, 143, 217, 353, 545, 857 GHz). Second, for each frequency, we added zero-mean Gaussian random noise with a frequency-dependent variance. In particular, the variance at frequency ν was fixed to the value $\sigma_\nu = \sigma_{217} * [1.66, 0.70, 1.00, 3.12, 19.50, 649.87]$[3], where σ_{217} is the standard deviation of the Gaussian noise in the 217 GHz map. Therefore, the simulated *Planck* noise maps are characterized by this single parameter σ_{217}.

---

[3] These ratios correspond to those of the real *Planck* maps in the SPT region.

Table 3. Joint S/N threshold q_J for different values of mean Poisson noise λ (expressed in counts/pixel), different values of mean Gaussian noise σ_{217} (in $\Delta T/T$ units), and several filter sizes (in arcmin).

$\theta_s = 0.8$	$\lambda = 0.03$	$\lambda = 0.06$	$\lambda = 0.09$	$\lambda = 0.15$	$\lambda = 0.25$	$\lambda = 0.40$	$\lambda = 0.70$	$\lambda = 2.00$	$\lambda = 7.50$
$\sigma_{217} = 10^{-5}$	7.31	5.67	5.09	4.71	4.59	4.52	4.50	4.51	4.51
$\sigma_{217} = 2 \times 10^{-5}$	8.84	7.02	6.21	5.45	4.94	4.70	4.55	4.50	4.52
$\sigma_{217} = 2.5 \times 10^{-5}$	9.15	7.40	6.57	5.77	5.17	4.84	4.61	4.53	4.53
$\sigma_{217} = 3 \times 10^{-5}$	9.34	7.64	6.84	6.03	5.38	4.98	4.69	4.54	4.55
$\sigma_{217} = 4 \times 10^{-5}$	9.55	7.95	7.17	6.38	5.69	5.23	4.86	4.60	4.56
$\sigma_{217} = 5 \times 10^{-5}$	9.65	8.10	7.36	6.59	5.93	5.44	5.01	4.65	4.57
$\sigma_{217} = 6 \times 10^{-5}$	9.71	8.20	7.47	6.72	6.08	5.58	5.15	4.70	4.59

$\theta_s = 5.19$	$\lambda = 0.03$	$\lambda = 0.06$	$\lambda = 0.09$	$\lambda = 0.15$	$\lambda = 0.25$	$\lambda = 0.40$	$\lambda = 0.70$	$\lambda = 2.00$	$\lambda = 7.50$
$\sigma_{217} = 10^{-5}$	6.19	5.14	4.79	4.60	4.52	4.43	4.42	4.42	4.42
$\sigma_{217} = 2 \times 10^{-5}$	7.06	5.96	5.50	5.07	4.76	4.55	4.44	4.41	4.38
$\sigma_{217} = 2.5 \times 10^{-5}$	7.23	6.17	5.72	5.25	4.92	4.65	4.52	4.44	4.41
$\sigma_{217} = 3 \times 10^{-5}$	7.34	6.32	5.87	5.40	5.05	4.76	4.58	4.48	4.43
$\sigma_{217} = 4 \times 10^{-5}$	7.47	6.49	6.06	5.59	5.23	4.92	4.71	4.53	4.46
$\sigma_{217} = 5 \times 10^{-5}$	7.52	6.58	6.17	5.70	5.35	5.04	4.81	4.58	4.49
$\sigma_{217} = 6 \times 10^{-5}$	7.56	6.64	6.23	5.76	5.43	5.14	4.90	4.63	4.51

$\theta_s = 30.0$	$\lambda = 0.03$	$\lambda = 0.06$	$\lambda = 0.09$	$\lambda = 0.15$	$\lambda = 0.25$	$\lambda = 0.40$	$\lambda = 0.70$	$\lambda = 2.00$	$\lambda = 7.50$
$\sigma_{217} = 10^{-5}$	5.11	4.54	4.40	4.18	4.21	4.17	4.01	4.10	4.10
$\sigma_{217} = 2 \times 10^{-5}$	5.51	4.97	4.67	4.43	4.50	4.39	4.23	4.28	4.22
$\sigma_{217} = 2.5 \times 10^{-5}$	5.59	5.06	4.74	4.52	4.60	4.44	4.29	4.36	4.26
$\sigma_{217} = 3 \times 10^{-5}$	5.63	5.11	4.80	4.58	4.64	4.48	4.34	4.43	4.28
$\sigma_{217} = 4 \times 10^{-5}$	5.66	5.16	4.88	4.65	4.69	4.51	4.40	4.51	4.28
$\sigma_{217} = 5 \times 10^{-5}$	5.68	5.17	4.91	4.69	4.70	4.52	4.45	4.56	4.28
$\sigma_{217} = 6 \times 10^{-5}$	5.69	5.18	4.94	4.71	4.70	4.54	4.49	4.58	4.26

Notes. These thresholds correspond to a false alarm rate of 3.4×10^{-6} (equivalent to a 4.5σ cut in a Gaussian distribution). They correspond to the case where exposure time is $400\,s$ and $N_H = 2 \times 10^{20}\,cm^{-2}$.

We repeated the experiment for different values of the mean Poisson level λ and the Gaussian noise level σ_{217}, and for each pair of values λ-σ_{217} we used 450 different realizations of the noise maps. At each realization, we changed the Poisson and the Gaussian noises (maintaining their levels), as well as the CMB realization.

Each set of $N_\nu + 1 = 7$ maps was then filtered using the proposed joint filter with the $N_s = 32$ different sizes, yielding the variance of the X-ray filtered map $\sigma^x_{\theta_s}$, the variance of the SZ filtered maps $\sigma^{sz}_{\theta_s}$, and the S/N map for each filter size.

From these results, we calculated the average values of $\sigma^x_{\theta_s}$ and $\sigma^{sz}_{\theta_s}$ corresponding to each noise level and filter size (see Tables 1 and 2). Finally, we established the joint S/N threshold q_J for a given λ-σ_{217}-θ_s triplet as the S/N value for which the fraction of pixels (considering the 450 realizations) with $S/N > q_J$ does not exceed a given false alarm probability P_{FA}. We used the number of pixels with $S/N > q_J$ as an approximation of the number of detections with $S/N > q_J$. Due to the iterative blind detection procedure, where each S/N peak is masked after detection (step 1b of the blind procedure described in Sect. 3.2), one detection spans more than 1 pixel. However, the approximation allows a much faster computation and it is also accurate enough, especially for small filter sizes, which is the regime where the Poisson noise peaks become more important and which we need to characterize better.

The value of P_{FA} serves to select the operational point of the detection method. The higher the P_{FA}, the lower the threshold q_J and the more candidates we keep, resulting in a catalogue with higher completeness and lower purity. On the contrary, if we want a very pure catalogue at the expense of being less complete, we can choose a small value of P_{FA}. Table 3 summarizes the S/N thresholds for each combination of noise and some filter sizes calculated for a false alarm rate of $P_{FA} = 3.4 \times 10^{-6}$, which corresponds to a cut at 4.5σ in a zero-mean Gaussian distribution.

For reasons of simplicity, we apply this adaptive threshold q_J after we have obtained the final candidate list from the second phase of the blind procedure. The threshold q to be applied in the first and second phases is established to a sufficiently low value so that it does not introduce any different selection effect, i.e. it does not discard any candidate above q_J. In our case, we selected $q = 4$ for the first and second phases, which is lower than any of the adaptive thresholds shown in Table 3. The adaptive threshold q_J is then used to discard noise detections in the following way.

1. For each detection in the final candidate list provided at the second phase of the joint blind algorithm, we save the joint S/N of the detection, the corresponding filter size θ_s, the standard deviation of the X-ray filtered map $\sigma^x_{\theta_s}$, and the standard deviation of the SZ filtered maps $\sigma^{sz}_{\theta_s}$;

2. We then calculate the mean Gaussian level $\hat{\sigma}_{217}$ that corresponds to the measured $\sigma_{\theta_s}^{sz}$ by interpolating in the simulation results (Table 2);

3. Then, we calculate the mean Poisson level $\hat{\lambda}$ that corresponds to the measured $\sigma_{\theta_s}^x$. To this end, we need to take into account that the measured $\sigma_{\theta_s}^x$ corresponds to a map with an exposure time and a N_H that are different from those used in the simulations ($t_{exp} = 400\,s$ and $N_H = 2 \times 10^{20}\,cm^{-2}$). Therefore, we will first convert the measured $\sigma_{\theta_s}^x$ into the value that we would have obtained with the values of exposure time and N_H used in the simulations, and then use Table 1 to interpolate the value of λ. The conversion from the measured $\sigma_{\theta_s}^x$ into its simulation-equivalent counterpart is done using Eq. (A.6). A detailed description of this conversion can be found in Appendix A;

4. We choose the two simulated values of σ_{217} that are closer to $\hat{\sigma}_{217}$ (one above: σ_{217}^+, one below: σ_{217}^-) and the two simulated values of λ that are closer to $\hat{\lambda}$ (λ^+ and λ^-). Then, we select the four simulations corresponding to the filter size θ_s and the four possible combinations of σ_{217}^+, σ_{217}^-, λ^+ and λ^-;

5. Then we calculate the S/N threshold for each of the four selected simulations. We cannot take the thresholds in Table 3 directly because they correspond to an X-ray map with $t_{exp} = 400\,s$ and $N_H = 2 \times 10^{20}\,cm^{-2}$ and the real map where we have detected the candidate will have, in general, different characteristics. To correct for this effect, we need to convert the S/N maps obtained in the simulations into equivalent S/N maps corresponding to the exposure time and N_H of the real map. This is done using Eq. (A.9), as explained in Appendix A. Then, for each of the four selected simulations, we calculate the S/N threshold as the value q_{Ji} for which the fraction of pixels on the transformed S/N maps with $S/N > q_{Ji}$ is at most P_{FA};

6. Finally, the threshold q_J to be applied to our detection is obtained via a 2D interpolation between the four values of q_{Ji}. If the S/N of the detection is above this threshold ($S/N > q_J$), we keep it in the list since it is not likely to be a noise detection (with confidence 1-P_{FA}); otherwise, we discard it.

3.4. Catalogue preparation

The blind detection outputs an all-sky catalogue of joint X-ray–SZ detections that may still contain non-cluster objects or detections caused by noise or contamination. As demonstrated in Tarrío et al. (2016), adding the X-ray information to the SZ maps increases the cluster detection probability, allowing us to detect fainter or more distant clusters with respect to the catalogues constructed from purely SZ information. However, introducing the X-ray maps also increases the number of false detections, produced by non-cluster X-ray sources (mainly AGNs) and Poisson noise. Furthermore, the SZ observations contain regions contaminated with infrared emission that may also produce false detections. Thus, a main challenge of the proposed X-ray–SZ blind detection is to obtain a high purity. To this end, the catalogue produced by the blind detection method needs to be cleaned to discard detections in contaminated regions of the sky, in regions with poor statistics, or that correspond to non-cluster objects. In the rest of this section, we introduce two masking procedures to avoid detections in regions with infrared contamination (Sect. 3.4.1) or X-ray poor statistics (Sect. 3.4.2), and a method for discarding real detections corresponding to non-cluster X-ray objects (Sect. 3.4.3).

3.4.1. SZ mask

To avoid SZ contaminated regions, we follow the same procedure used to build the second *Planck* cluster catalogue (PSZ2) described in Planck Collaboration XXVII (2016), i.e. we discard all the detections inside the PSZ2 survey mask, we also reject detections within $5\sigma_{beam}$ of any SZ compact source of the second *Planck* catalogue of compact sources (PCCS2; Planck Collaboration XXVI 2016) with $S/N > 10$ in any of the six HFI *Planck* channels, and we remove 7 arcmin matches with the *Planck* cold-clump catalogue (C3PO), or with PCCS2 detections at both 545 GHz and 857 GHz to eliminate spurious infrared detections.

3.4.2. X-ray mask

In the regions of the sky where the X-ray exposure time is very low, the X-ray count-rate map contains few noise pixels with very high count-rate values (typically, one count divided by a very low exposure time) compared to adjacent pixels (with zero counts). These bright pixels may introduce false detections, which could be discarded using the adaptive threshold calculated by numerical simulations. However, since the amount of simulation time required to properly simulate these regions is significant, and given that the X-ray information provided by these regions is very limited, we decided to just set a threshold in the exposure time to mask the low-exposure regions. In the case of RASS, we decided to use a threshold of 100 s, which masks only 5.5% of the sky, i.e. 2300 deg^2, where 910 deg^2 have a non-zero exposure time and 1390 deg^2 have no RASS observations. The overlap of this masked area with the SPT footprint, where the proposed method will be evaluated (see Sect. 4), is 209 deg^2, 80 deg^2 with non-zero exposure time and 129 deg^2 with no RASS observations.

### 3.4.3. Classification to distinguish clusters from point sources

Some of the objects detected with the blind joint detection method correspond to point sources in the X-ray maps that coincide with a SZ noise peak. Although the estimated size can be used as a criterion to distinguish between a real cluster and a point source, it is difficult to distinguish between a cluster with a small apparent size and a point source.

Our ideal aim would be to recognize whether a detection is a real cluster or a point source given the parameters extracted during the filtering process. To check if this is possible, we cross-matched some joint detections with a list of known clusters and known point sources (see details below), and we labelled each of our matching candidates as belonging to one or the other class. Then, we characterized each sample of this labelled list using five features: the estimated S/N, size and flux of the blind joint detection, and the X-ray and SZ components of the S/N: $(S/N)_{XR}$ and $(S/N)_{SZ}$. Finally, in order to get an upper bound on the best classification accuracy that can be obtained with a linear classifier, we trained a support vector machine (SVM) classifier with this labelled list.

Using ten-fold cross-validation[4], we obtained a classification accuracy of 88%, with 5% of the mis-classifications being point sources classified as clusters and 7% being clusters classified as point sources. We noticed that the parameter that plays the most

---

[4] The dataset is randomly divided into ten subsets. Then, nine subsets are used to train the SVM and one is used to test the classifier. This validation process is repeated ten times; each subset is used only once as test set, and the ten results are averaged.
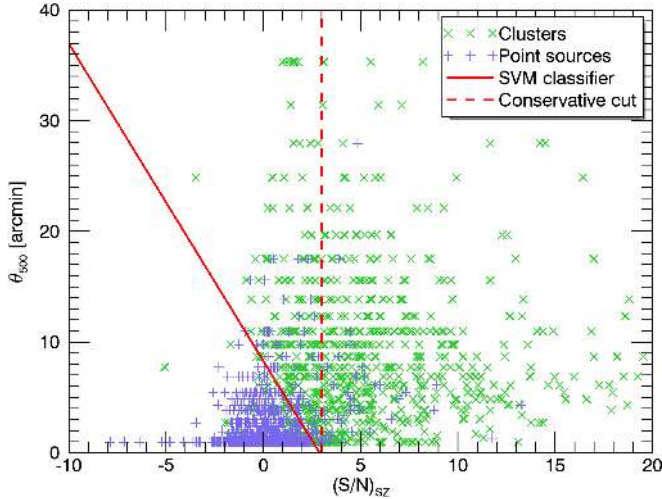
Fig. 2. Estimated $(S/N)_{SZ}$ and size θ_{500} of the joint detections in the northern hemisphere that match a known cluster or a known X-ray point source. The continuous red line shows the classification boundary provided by a SVM classifier trained with this dataset. The dashed red line shows the conservative cut that we adopted for discarding point sources.

important role in the classification is $(S/N)_{SZ}$, followed by the estimated size θ_{500}. This is logical because we do not expect to find an SZ signal at the position of an AGN, and we expect them to be small (they are point-like sources). A classification considering only these two parameters gives the same performance as the one obtained with the five parameters. Figure 2 shows the detections used for this experiment in the $(S/N)_{SZ}$–θ_{500} plane, colour-coded according to the type of object with which they are associated. A red line indicates the best linear classification boundary determined by the trained SVM. A simple classification boundary of $(S/N)_{SZ} = 2$ provides almost the same performance as the complete SVM classifier: 85% correct classifications, with 4% of the point sources classified as clusters and 11% of the clusters classified as point sources. So, for simplicity reasons, we decided to use only $(S/N)_{SZ}$ for the cluster/point source classification. Finally, since for our purity purposes we prefer to have fewer false clusters at the expense of a lower classification accuracy (and thus, lower completeness), we decided to modify the classification threshold to $(S/N)_{SZ} = 3$, which provides 82% correct classifications, with only 2% of the point sources classified as clusters (and 16% of the clusters classified as point sources).

As mentioned before, the classification is based on the labels obtained by cross-matching some joint detections with a list of known clusters and known point sources. In particular, to construct the list of known clusters we used the MCXC (Piffaretti et al. 2011), ESZ (Planck Collaboration VIII 2011), PSZ1 (Planck Collaboration XXIX 2014), PSZ2 (Planck Collaboration XXVII 2016), SPT (Bleem et al. 2015b), and ACT (Hasselfield et al. 2013) cluster catalogues, and considered only confirmed clusters. Figure 3 shows the distribution of redshift, mass, and size of these clusters. To construct the list of known point sources, we took the ROSAT bright source catalogue (Voges et al. 1999) and we applied the selection criteria of MACS (Ebeling et al. 2001). All the objects in the resulting list were followed up for confirmation by MACS, so by eliminating the objects that match with a known cluster, we were left with a list of X-ray point sources. Since all these point sources belong to the northern hemisphere, the list of joint detections that we used for this test was obtained by running the joint

detection algorithm on the northern hemisphere. Then, we then cross-matched our list of detections with the two lists to label our detections as clusters or point sources. This cross-match was done based on distance, with a matching radius of 2 arcmin. It is worth mentioning that this labelling may not be completely accurate, first because the catalogues of known point sources and clusters may not be completely correct, and second because the cross-matching done according to distance may introduce some incorrect matches. Therefore, the classification results reported above just provide a good idea of the real classification performance (with respect to the unknown ground truth). Finally, we want to emphasize that these classification results are based on the selected training dataset, so they cannot be generalized to the problem of distinguishing point sources from any kind of cluster.

3.5. Output parameters and mass estimation

For each detection, the joint algorithm provides its position, the size θ_{500} of the filter that gives the best joint S/N, the corresponding flux Y_{500} and joint S/N, and the SZ and X-ray components of this S/N: $(S/N)_{SZ}$ and $(S/N)_{XR}$.

Additionally, the joint method also provides a value for the significance of each detection. This value is calculated from the simulation results described in Sect. 3.3 in the following way:

1. For each detection, we select the four simulations corresponding to the filter size that are closer to the mean Poisson level λ and mean Gaussian level σ_{217} of the analysed map, and we convert the S/N maps obtained in the simulations into equivalent S/N maps corresponding to the exposure time and N_H of the real map, as in steps 1 to 3 of Sect. 3.3;

2. Then, we calculate the fraction of pixels in the simulations with a S/N on these transformed S/N maps greater than the joint S/N of the detection. This measures the probability of a false detection;

3. Finally, we perform a 2D interpolation using these four values to obtain the probability that the detection is due to noise. From this probability, we calculate the value of significance corresponding to a Gaussian distribution;

4. We note that if the joint S/N is very high, there are no pixels in the simulations with a higher S/N. In these cases, it is not possible to calculate the significance directly, and we use the following expression to estimate it: significance = $4.5 + 0.68 \cdot ((S/N)_J - q_J)$. Appendix B explains how this expression was obtained.

Finally, since the size estimation is not very accurate, as occurred for PSZ2 catalogue, the blind detection provides the degeneracy curves $Y_{500}(\theta_{500})$ and $(S/N)_J(\theta_{500})$ for the assumed reference redshift z_{ref}, which allow us to determine more precisely the size and flux of the cluster given some a priori information about the cluster (e.g. redshift).

Apart from the degeneracy curve $Y_{500}(\theta_{500})$ corresponding to the reference redshift z_{ref}, we can also re-extract the degeneracy curves for different redshifts at the position given by the blind detection. Then, if the detection matches a cluster with known redshift, we can interpolate between these degeneracy curves to obtain the curve corresponding to the real redshift of the cluster. This size–flux degeneracy can be further broken using the $M_{500} - D_A^2 Y_{500}$ relation, which relates θ_{500} and Y_{500} when z is known, as explained in Sect. 7.2.2 of Planck Collaboration XXIX (2014). In this way, we can obtain an estimate of the mass M_{500} of the candidate. In Sect. 3.5 we compare the mass estimated
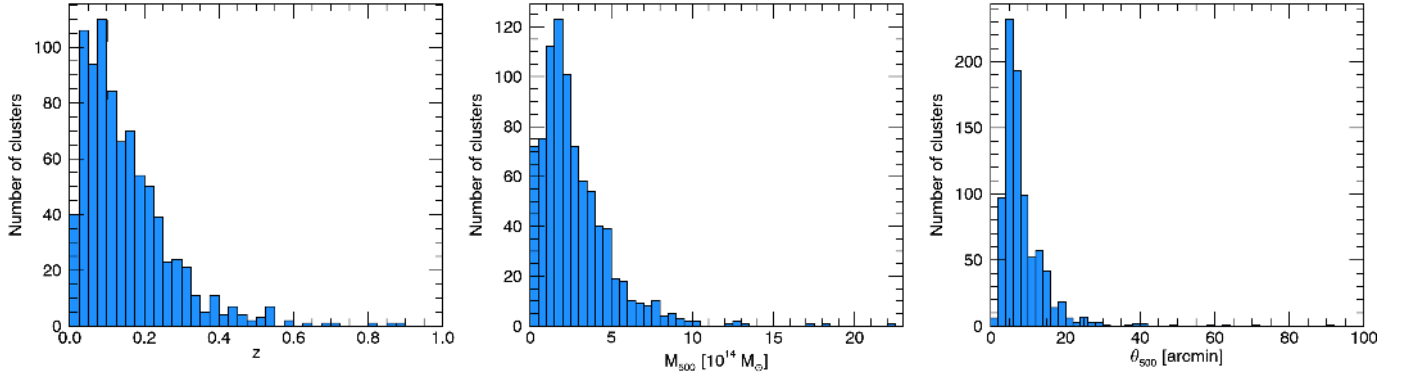
Fig. 3. Distributions of the redshift (*left*), mass (*middle*), and size (*right*) of the clusters used for the training of the SVM classifier.

4. Evaluation in SPT area

In this section we present an evaluation of the proposed blind detection method in the region of the sky covered by the SPT survey. This region was selected because it is a wide-area region of the sky (2500 deg^2) where we can assume that almost all the massive clusters ($M_{500} > 7 \times 10^{14} M_\odot$) up to redshift 1.5 are already known. On the one hand, the SPT survey, which is deeper than the *Planck* survey, is almost 100% complete at $z > 0.25$ for clusters with mass $M_{500} > 7 \times 10^{14} M_\odot$ (Bleem et al. 2015b) (~90% complete for $M_{500} > 6 \times 10^{14} M_\odot$). On the other hand, the X-ray MCXC catalogue (Piffaretti et al. 2011) should include almost all the clusters with mass $M_{500} > 5 \times 10^{14} M_\odot$ at $z < 0.25$ since it contains the REFLEX sample, which is highly complete (>90%) for that redshift-mass range (see Fig. 10). There is however a small redshift range around 0.2–0.3 where some massive clusters could be still unknown. Less massive clusters could also be unknown in a broader redshift range. A comparison of the blind detection results with these catalogues allows us to determine whether the detected candidates are real clusters (purity) and what fraction of real clusters we actually detect (detection efficiency). Nevertheless, we should keep in mind that there could be some clusters in the transition region that are neither in SPT nor in MCXC. Also, other clusters could be missing due to masked regions in the surveys.

We ran the blind joint detection algorithm on the SPT footprint[5] and obtained 2767 detections in the second phase (using $q = 4$). Then, we applied the cuts in the *Planck* S/N ($S/N_{SZ} > 3$), the RASS exposure time ($t_{exp} > 100$ s) and the joint S/N ($S/N_J > q_J$), and we applied the SZ cleaning procedure described in Sect. 3.4.1. If we choose a false alarm rate of $P_{FA} = 3.40 \times 10^{-6}$ to calculate the joint S/N threshold q_J to apply to the 2767 detections, we are left with 225 candidates. Table C.1 summarizes the properties of these candidates. If we decrease this false alarm probability we get fewer candidates; for example, for $P_{FA} = 2.04 \times 10^{-7}$ (equivalent to a 5σ cut in a Gaussian distribution) we get 185 candidates and for $P_{FA} = 1.90 \times 10^{-8}$ (equivalent to a 5.5σ cut in a Gaussian distribution) we get 165 candidates.

The detection area is not covered homogeneously: there are slightly more candidates in the regions where the RASS exposure time is higher and where the *Planck* noise is lower. This is

---

[5] Defined as (RA < 104.8° or RA > 301.3°) and −65.4° < Dec < −39.8°.
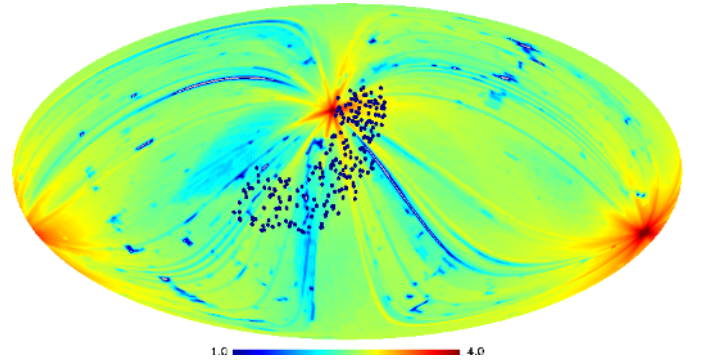
Fig. 4. Positions of the joint detections with respect to the RASS exposure map. Blue dots represent the 225 candidates corresponding to a false alarm rate of $P_{FA} = 3.40 \times 10^{-6}$. The sky map is colour-coded according to the logarithm of the RASS exposure time.
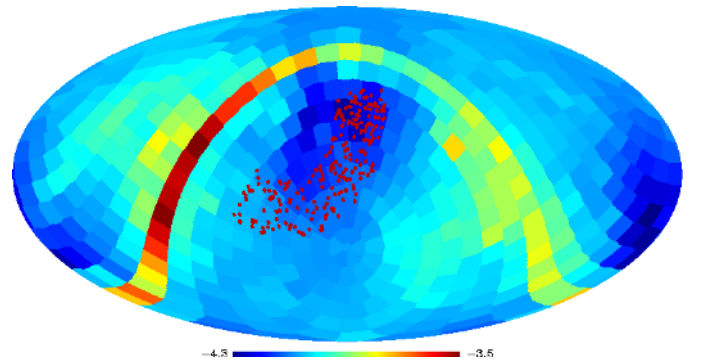
Fig. 5. Positions of the joint detections with respect to the *Planck* noise map. Red dots represent the 225 candidates corresponding to a false alarm rate of $P_{FA} = 3.40 \times 10^{-6}$. The sky map is colour-coded according to the logarithm of the *Planck* noise standard deviation map.

expected, since in those regions both surveys are deeper. This effect is shown in Figs. 4 and 5.

4.1. Crossmatch with other cluster catalogues

To estimate the purity and the detection efficiency of these catalogues, we cross-matched all the candidates with various published catalogues of clusters. In particular, we took several SZ-selected catalogues covering the considered region, namely the three *Planck* catalogues: ESZ (Planck Collaboration VIII 2011), PSZ1 (Planck Collaboration XXIX 2014), and PSZ2 (Planck Collaboration XXVII 2016), the SPT catalogue
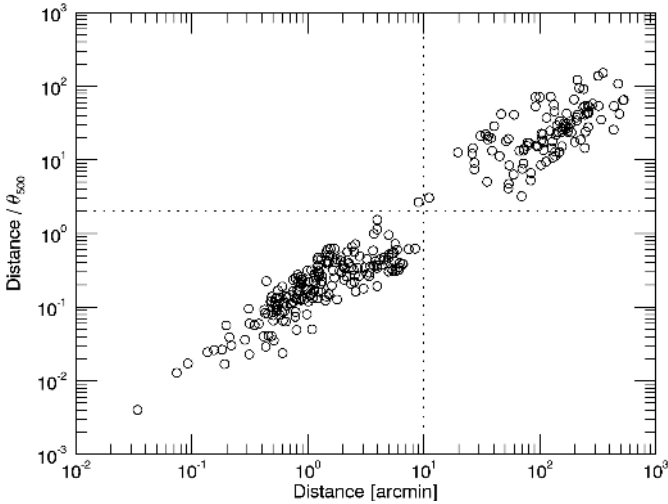
Fig. 6. Distance from the joint position to the position of the closest cluster vs. the distance normalized to the cluster size. Only the objects with known redshift and mass in the considered SZ and X-ray catalogues were taken as clusters.

(Bleem et al. 2015b), and the ACT catalogue (Hasselfield et al. 2013). It is worth mentioning that a subsample of the PSZ2 catalogue, namely the MMF3 sub-catalogue, is especially interesting for us since the proposed joint detection method is based on the MMF3 detection method. The SPT and ACT surveys are deeper than the *Planck* survey, so these catalogues contain additional clusters that were not detected by *Planck*. We also took as reference the X-ray selected MCXC catalogue (Piffaretti et al. 2011). This is a metacatalogue of X-ray detected clusters that was constructed from publicly available cluster catalogues of two kinds: RASS-based catalogues, obtained from the RASS survey data, and serendipitous catalogues, based on deeper pointed X-ray observations. Finally, we also considered the optically selected Abell catalogue (Abell et al. 1989). We did not use the Zwicky and redMaPPer catalogues since they do not contain clusters in the considered region.

To decide whether our detections match these previously known candidates, we first determined the closest cluster to each of our detections. To this end, we selected only the objects in the considered SZ and X-ray catalogues with known redshift and mass (i.e. confirmed clusters). Figure 6 shows a scatter plot of the absolute distance versus the relative distance (in terms of θ_{500}) between the associated objects. We observe two types of associations: those with a small distance in absolute and in relative terms, and those with a long distance in absolute and in relative terms. The first group of points represents true detections of clusters, whereas the second group corresponds to the detections that are randomly distributed with respect to the considered known clusters. From this observation, we decided to use the following association rule: if the distance is <10 arcmin the detection is considered as associated with a known cluster, otherwise the detection is considered as not associated with a known cluster. We show in Sect. 4.2 that the resulting associations are valid, since the masses of the detected objects and the associated clusters agree. Furthermore, given that the considered catalogues also contain objects without redshift and mass information, we decided not to introduce an additional criterion based on the relative distance, which can be only calculated if the θ_{500} of the object is known. This association rule is very simple, but has the advantage that it can be applied to all the candidates in the considered catalogues.

After the cross-match of our candidates with these published catalogues, we found that 187 of the 225 detections corresponding to $P_{FA} = 3.40 \times 10^{-6}$ match a previously known confirmed cluster within a distance of 10 arcmin. This corresponds to a purity >83.1%. For the case of $P_{FA} = 2.04 \times 10^{-7}$ we found that 166 of the 185 detections match a previously known confirmed cluster, whereas for $P_{FA} = 1.90 \times 10^{-8}$ there are 151 matches out of 165 detections. This corresponds to a purity >89.7% and >91.5%, respectively, which is higher than before, as expected, since we decreased the false detection probability. Table 4 shows more details about the number of candidates matching the different cluster catalogues that we considered.

In this context, and for the rest of this section, we have defined "purity" as the percentage of joint detections that are associated with a confirmed cluster in these published catalogues. It is important to keep in mind that these values of purity are just rough estimations since our simple association rule could introduce a few incorrect associations. Furthermore, the candidates without a match may also be real clusters that have not been detected or included in the published catalogues (objects in masked regions, objects in a mass-redshift region where the considered surveys are not complete, etc.). Therefore, the value of purity with respect to previously known confirmed clusters can be considered an approximate lower limit.

On the other hand, we define "detection efficiency" as the percentage of candidates in the considered published catalogues that are detected by our joint algorithm. This magnitude is related to the completeness. To calculate it, we have cross-matched all the previously known clusters in the considered region (SPT region with RASS exposure time >100 s, outside the PSZ2 masked region) with our detections. Table 4 shows the results from this cross-match for different values of P_{FA}. A higher P_{FA} allows us to recover more clusters, but at the expense of a lower purity, as seen at the bottom line of Table 4. As expected, the proposed method is able to recover most of the MMF3 objects, given that it is based on the same data and a similar approach. A more detailed comparison with respect to MMF3 can be found in Sect. 4.4. The recovery rate of PSZ2 and *Planck* clusters is also high. On the contrary, the method recovers only a small fraction of SPT clusters not detected by *Planck*, which was foreseen, since the SPT survey data is deeper. Finally, 68.9% of the RASS clusters situated in the considered region are recovered. Given that the proposed method also uses RASS observations, this value may seem low; however, it is not due to the detection algorithm, but to the additional cut we imposed to discard possible X-ray point sources. A more detailed comparison with respect to RASS clusters can be found in Sect. 4.5.

4.2. Mass comparison

Following the procedure described in Sect. 3.5 and using the $M_{500} - D_A^2 Y_{500}$ relation proposed in Planck Collaboration XX (2014), we estimated the mass M_{500} for the detections matching confirmed SZ or MCXC clusters. There are a total of 163 detections matching a confirmed SZ cluster (155 with known mass) and 72 detections matching MCXC clusters. Figure 7 shows the relation between the estimated mass and the published mass for the corresponding clusters.

The comparison with respect to the published SZ mass (Fig. 7a) shows that the estimated mass closely follows the published mass; the median ratio is 0.98, very close to 1. We identified four outliers that are at more than 2.5σ from the median ratio, two with overestimated masses and two with

Table 4. Number of previously known clusters or cluster candidates in the considered region that match our detections for $P_{FA} = 3.40 \times 10^{-6}$, $P_{FA} = 2.04 \times 10^{-7}$, and $P_{FA} = 1.90 \times 10^{-8}$ within a distance of 10 arcmin.

Cluster catalogue	Clusters in the considered region	$P_{FA} = 3.40 \times 10^{-6}$		$P_{FA} = 2.04 \times 10^{-7}$		$P_{FA} = 1.90 \times 10^{-8}$	
		Clusters detected	Percentage (%)	Clusters detected	Percentage (%)	Clusters detected	Percentage (%)
All MMF3	126	118	93.7	111	88.1	106	84.1
Confirmed MMF3	113	110	97.3	106	93.8	102	90.3
MMF3 candidates	13	8	61.5	5	38.5	4	30.8
All PSZ2	154	133	86.4	124	80.5	117	76.0
Confirmed PSZ2	131	125	95.4	120	91.6	114	87.0
PSZ2 candidates	23	8	34.8	4	17.4	3	13.0
All *Planck*	174	134	77.0	125	71.8	118	67.8
Confirmed *Planck*	137	126	92.0	121	88.3	115	83.9
Planck candidates	37	8	21.6	4	10.8	3	8.1
Confirmed SPT	494	111	22.5	98	19.8	89	18.0
ACT	22	16	72.7	14	63.6	14	63.6
MCXC	138	72	52.2	72	52.2	72	52.2
RASS	103	71	68.9	71	68.9	71	68.9
Abell	896	104	11.6	96	10.7	91	10.2
MCXC not SZ	70	9	12.9	9	12.9	9	12.9
confirmed SPT not *Planck*	405	32	7.9	23	5.7	18	4.4
All SZ	734	163	22.2	146	19.9	134	18.3
Confirmed SZ	544	155	28.5	142	26.1	131	24.1
SZ candidates	190	7	3.7	3	1.6	2	1.1
All SZ + MCXC	804	172	21.4	155	19.3	143	17.8
Confirmed SZ + MCXC	614	164	26.7	151	24.6	140	22.8
SZ + MCXC candidates	190	10	3.7	3	1.6	2	1.1
Total number of detections		225		185		165	
Detections matching any confirmed cluster		187		166		151	
Purity (w.r.t. confirmed clusters)		>83.1%		>89.7%		>91.5%	

Notes. *Planck* refers to the combination of the three *Planck* catalogues (Planck Collaboration VIII 2011; Planck Collaboration XXIX 2014; Planck Collaboration XXVII 2016), whereas PSZ2 refers only to the last one. MMF3 is the subsample of objects in the PSZ2 catalogue that were detected using the MMF3 detection algorithm. RASS refers to the subsample of objects in the MCXC catalogue that were detected from RASS observations. SZ refers to the combination of all the SZ catalogues (*Planck*, SPT, and ACT).

underestimated masses. Figure 7a also shows that the SPT clusters that were not detected by *Planck* have, on average, a higher mass ratio than those detected by *Planck*. This behaviour can be explained by the Malmquist bias.

The two outliers with overestimated mass correspond to clusters PSZ2 G252.99-56.09 (also RXC J0317.9-4414, ABELL 3112) and PSZ2 G348.46-64.83 (also SPT-CLJ2313-4243, RXC J2313.9-4244, and ACO S 1101). Both clusters are known strong cool-cores according to the classification of Hudson et al. (2010), so the assumed F_X/Y_{500} relation used in the detection does not represent these clusters accurately. Since our mass estimation is obtained from the combination of X-ray and SZ information, its value compared to the SZ mass is boosted due to the high X-ray luminosity. We checked that the estimated mass using only the SZ information agrees with the published mass, which supports this explanation.

The two outliers with underestimated masses correspond to clusters PSZ2 G265.21-24.83 (also RXC J0631.3-5610) and PSZ2 G269.36-47.20 (also RXC J0346.1-5702 and ABELL 3164). They can be justified by the high distance between the joint detection and the published position, which is 8.4 and 7.4 arcmin, respectively. This implies that the SZ signal at the

detected position is not at its peak value, which explains the low value obtained for the mass. The reason for this distance is that the detection is centred on the X-ray peak, while the X-ray emission is not coincident with the SZ emission, as can be seen in Fig. 8. We note that in both cases the distance normalized by the cluster size is <1, so the association can be still considered correct.

The comparison with respect to the published MCXC mass (Fig. 7b) shows that the ratio between the estimated mass and the published mass is >1, with a median value of 1.19. The same value is found for the ratio between the published SZ mass and the published MCXC mass for the same clusters. This behaviour was also observed by the Planck Collaboration XXVII (2016) when they compared the SZ mass and the X-ray luminosity of common PSZ2-MCXC objects. We identified two outliers that are at more than 2.5σ from the median ratio. They coincide with the two outliers with underestimated mass with respect to published SZ mass (Fig. 7a).

This mass comparison indicates that the joint extraction provides in general a good mass proxy when the redshift is known. The main sources of bias in the mass estimation are the presence of a cool core, which tends to overestimate the mass, and
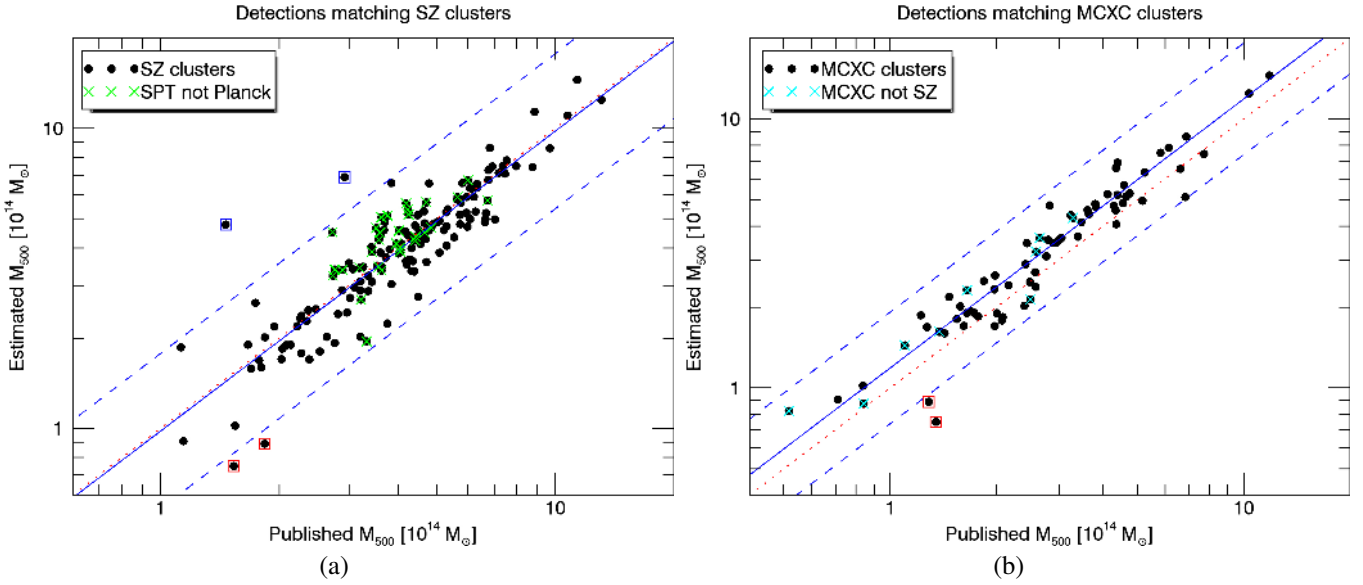
Fig. 7. M_{500} estimated from the joint detection for the candidates matching a confirmed cluster vs. the published M_{500} of the corresponding cluster. *Panel a*: comparison of the estimated mass to the published SZ mass for the 155 candidates matching an SZ cluster with known mass. *Panel b*: comparison of the estimated mass to the published MCXC mass for the 72 candidates matching an MCXC cluster. The dotted red line indicates the line of zero intercept and unity slope. The solid blue line indicates the median ratio. The dashed blue lines indicate the interval of $\pm 2.5\sigma$ around the median ratio. Outliers are highlighted with a blue (high estimated mass) or red (low estimated mass) square; see text. Green crosses indicate SPT clusters that are not in *Planck* catalogues and cyan crosses indicate MCXC clusters that are not in *Planck* or SPT.
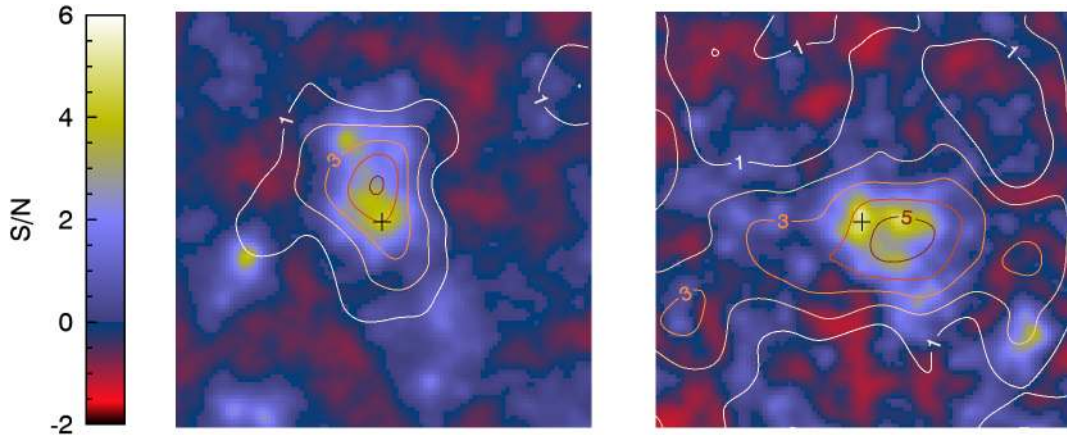
Fig. 8. S/N maps for the two outliers with underestimated mass with respect to the published SZ mass and X-ray mass: PSZ2 G265.21-24.83 (*left*) and PSZ2 G269.36-47.20 (*right*). The colour images show the S/N corresponding to the X-ray map and the contours indicate the S/N corresponding to the SZ maps. The black crosses indicate the positions of the joint detection. The angular size of the images is 86.7 arcmin. The distance between the joint detection and the published SZ position is 8.4 and 7.4 arcmin, respectively.

an offset between the X-ray and SZ peaks, which tends to give underestimated masses.

The good agreement between the estimated and the published masses also indicates that the 10 arcmin association rule is appropriate.

4.3. Position accuracy

Since the proposed method combines *Planck* maps with RASS observations, which have better position accuracy due to the smaller beam, we expect the positions provided by the joint detection method to be more accurate than those provided by *Planck*. To assess this accuracy, we took as reference the positions given in the SPT catalogue, which are more accurate than *Planck* positions. Then, we selected the joint detections that match clusters detected both by SPT and PSZ2 and calculated

the distance between the joint position and the SPT position. Finally, we compared this distance to the distance between the SPT and the PSZ2 position for the same clusters. Figure 9 summarizes this comparison. On average, the joint position is closer to the SPT position than the PSZ2 position is. Therefore, we can conclude that the joint detection method introduces a gain in the position determination with respect to *Planck*, thanks to the use of the X-ray information.

4.4. Performance comparison with the MMF3 method

Since the proposed joint detection method is built as an extension of the MMF3 detection method, we expect it to have a better performance than that of its predecessor.

As shown in Table 4, the proposed method is able to recover most of the MMF3 candidates for $P_{FA} = 3.40 \times 10^{-6}$ and only
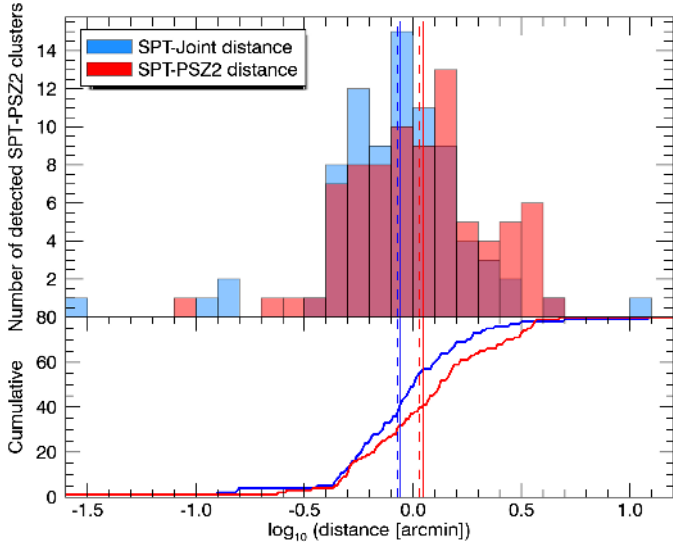
Fig. 9. Distance between the SPT and joint positions (blue) and between the SPT and PSZ2 positions (red). The median and mean values of each set of distances are represented by solid and dashed lines, respectively. *Upper panel*: histograms. *Lower panel*: corresponding cumulative distributions.

eight MMF3 candidates are missing, three of which are confirmed clusters. The three missing clusters were initially detected (in the second phase), but then were discarded because the joint S/N was not high enough. The five MMF3 unconfirmed clusters that do not appear in our candidate list are missing for several reasons: two of them are below the initial threshold $q = 4$ used to include S/N peaks in the list, one has a joint S/N lower than the corresponding threshold q_J, and two were discarded because they have a $(S/N)_{SZ} < 3$. These five objects belong to the PSZ2 catalogue, but they are not detected by SPT or ACT, and they do not have any known external counterpart. The recovery rate for MMF3 confirmed clusters is much higher than that of MMF3 candidates, which indicates that thanks to the combination with the X-ray information, our joint detection is able to clean the MMF3 catalogue of non-cluster objects.

Even though the proposed method misses a small fraction of the MMF3 clusters, it detects other previously known clusters that are missed by MMF3 (see Table 4). In particular, for $P_{FA} = 3.40 \times 10^{-6}$, it detects 16 additional *Planck* clusters, 32 SPT clusters that were not detected by *Planck*, and 9 MCXC clusters that were not detected by *Planck* or SPT. The overall effect is an improvement of the purity-detection efficiency performance with respect to the reference method MMF3. A comparison of the two methods can be seen in Fig. 10, which shows the MMF3 clusters and the joint detections in the mass-redshift plane for $P_{FA} = 3.40 \times 10^{-6}$ and $P_{FA} = 2.04 \times 10^{-7}$. The MMF3 clusters are represented as black open circles, whereas the joint detections are represented as coloured symbols. For $P_{FA} = 3.40 \times 10^{-6}$, the proposed method is able to recover almost all the MMF3 clusters while detecting at the same time additional clusters down to a mass of $2.6 \times 10^{14} M_\odot$ at redshift 0.5. For $P_{FA} = 2.04 \times 10^{-7}$, the proposed method recovers fewer clusters due to the increased purity.

Figures 11 and 12 show two examples of additional clusters detected by the proposed method thanks to the combination of SZ and X-ray information. Figure 11 shows SPT-CLJ0351-4109, a cluster at $z = 0.68$ with $M_{500} = 4.26 \times 10^{14} M_\odot$ detected by SPT, but not detected by *Planck*. The SZ S/N obtained from

Planck observations is too low to pass the *Planck* detection threshold. However, the presence of some X-ray photons at the same position (11 photons within a 4 arcmin-radius circle, compared to 3.5 photons expected from the average background level) boosts the joint S/N so that the cluster is detected. The red smooth region on the right side of the middle panel of Fig. 11 is due to a negative ripple introduced by the filter around a very strong X-ray source (X-ray S/N of 75.4) situated to the right of the cluster, at a distance of 39 arcmin (outside the region represented here). Figure 12 shows RXC J0211.4-4017, a cluster at $z = 0.1$ with $M_{500} = 1.65 \times 10^{14} M_\odot$ included in the MCXC catalogue, but not detected by *Planck* or SPT. In this case, the presence of a strong X-ray signal at the same position of a faint SZ signal allows the detection of this cluster.

A direct comparison of the purity-detection efficiency performance of the joint detection method and MMF3 can be seen in Fig. 13. The purity and the detection efficiency are calculated with respect to all confirmed clusters from *Planck*, SPT, and MCXC catalogues in the considered region, thus, they are both rough estimations. Nevertheless, they serve as indicators to compare our method with the reference MMF3. The figure shows different operational points of both methods. For MMF3, the operational point is chosen through the S/N threshold. For the nominal *Planck* catalogue, this threshold is set to 4.5, but different thresholds can be used, producing catalogues with different purity and detection efficiency (thus, different completeness). The proposed joint method can be tuned by changing the false alarm probability that is used to calculate the joint S/N threshold. This figure shows that our detection method outperforms MMF3 in the sense that it can simultaneously achieve higher purity and higher detection efficiency if the operational point is chosen appropriately.

4.5. Comparison with RASS clusters

Since the proposed joint detection method uses RASS observations, it is interesting to check whether it is able to recover known clusters that have been detected using the same observations. Table 4 shows that we detect 71 of the 103 RASS clusters situated in the considered region (SPT area with RASS exposure time >100 s, outside the PSZ2 masked region), which corresponds to 68.9%. Most of the RASS clusters that we do not recover (30 of the 32) were in fact included in the list of detections provided by the second phase of the algorithm, but 29 were discarded because their $(S/N)_{SZ}$ was lower than 3 and one was discarded because the RASS exposure time at the detection's position is lower than 100 s. There are just two RASS clusters that were not originally detected by the joint algorithm because their joint S/N does not reach the threshold of $q = 4$: RXC J0040.1-5607 and RXC J2326.7-5242, which are quite faint both in X-ray and SZ. To cross-check these results, we used the MMF3 method of Planck Collaboration XXVII (2016) to extract the S/N of RASS clusters from *Planck* maps. We found that the 2 undetected clusters and the 29 clusters that were discarded due to a low $(S/N)_{SZ}$ have a very low S/N, which supports our results. Therefore, we can conclude that the joint detection method is able to recover almost all the RASS clusters, as expected, but we discard some of them later in order to maintain a high purity by eliminating possible AGN detections with a threshold in $(S/N)_{SZ}$, which has a similar effect to a mass cut at each redshift. Figure 14 illustrates this comparison by showing the RASS clusters and the joint detections in the mass-redshift plane.

Pfa = 3.4e-6 (4.5 sigma)

(a)

Pfa = 2e-7 (5 sigma)

(b)
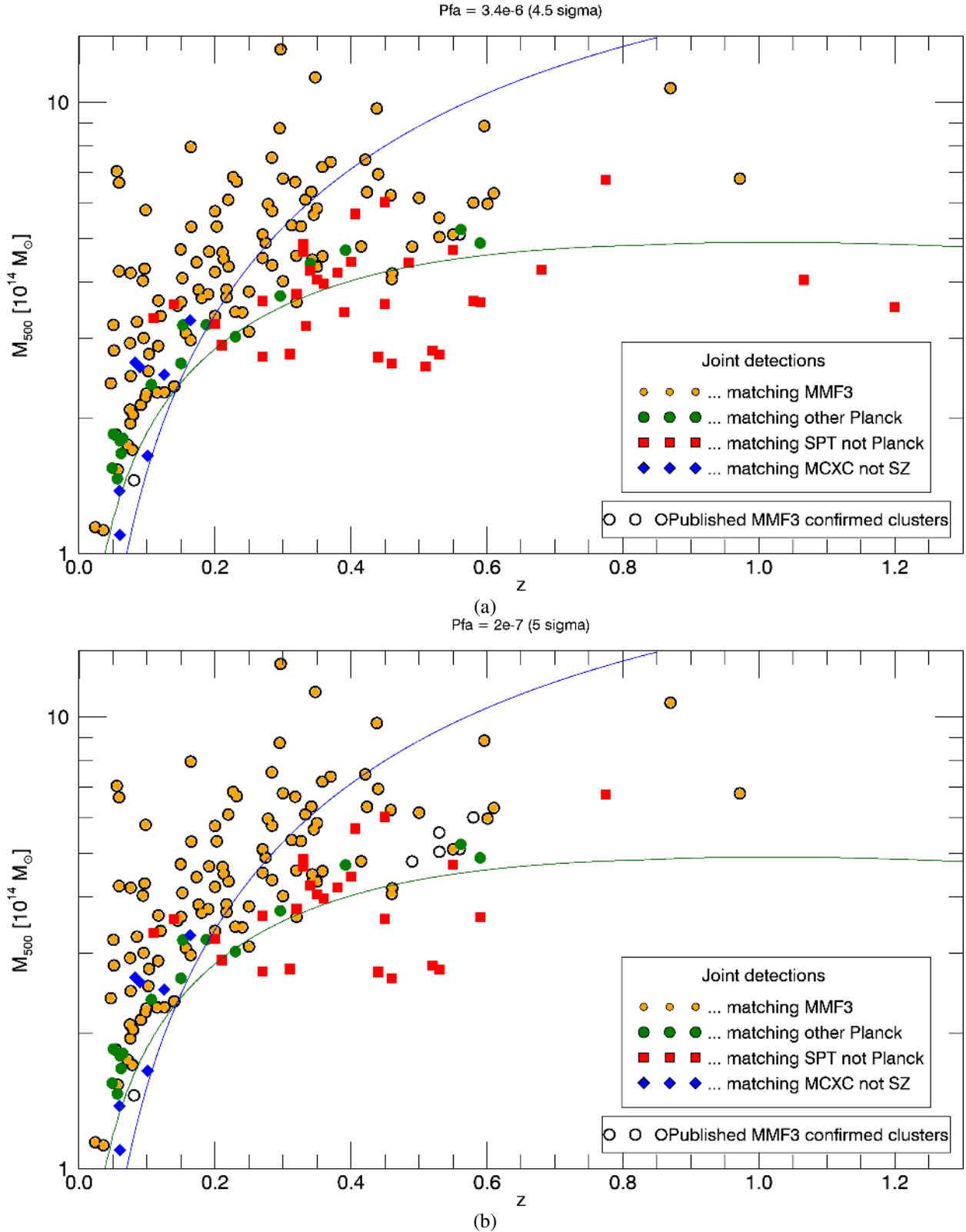
Fig. 10. Mass and redshift of the clusters in the MMF3 catalogue and of the clusters detected with the proposed method for (*a*) $P_{FA} = 3.40 \times 10^{-6}$ and (*b*) $P_{FA} = 2.04 \times 10^{-7}$. Open circles represent the MMF3 confirmed clusters in the considered region, while filled symbols represent the joint detections colour-coded according to the associated cluster. Yellow filled circles represent joint detections matching confirmed MMF3 clusters, green filled circles represent joint detections matching other confirmed *Planck* clusters (not MMF3), red squares represent joint detections matching confirmed SPT clusters not detected by *Planck*, and blue diamonds represent joint detections matching confirmed MCXC clusters that do not match any of the previously mentioned catalogues. The blue solid line shows the REFLEX detection limit, calculated from the REFLEX flux limit and the $L_X - M_{500}$ relation presented in Piffaretti et al. (2011). It corresponds to a completeness of at least 90% (Böhringer et al. 2001). The green solid line shows the *Planck* mass limit for the SPT zone at 20% completeness.
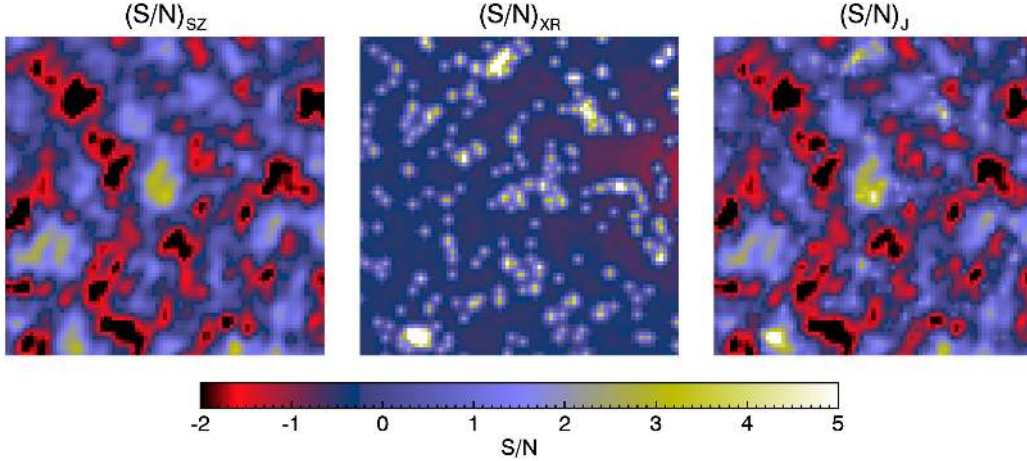
Fig. 11. S/N maps for the joint detection that matches SPT-CLJ0351-4109, an SPT cluster not detected by *Planck* situated at $z = 0.68$ with $M_{500} = 4.26 \times 10^{14} \, M_\odot$. The three colour images show the S/N corresponding to the SZ filtered maps (*left*), the X-ray filtered map (*middle*), and the joint filtered maps (*right*). The filter size is 0.8 arcmin, which provides the best S/N for this detection. The angular size of the images is 68.7 arcmin. The RASS exposure time at the position of the detection is 545 s.
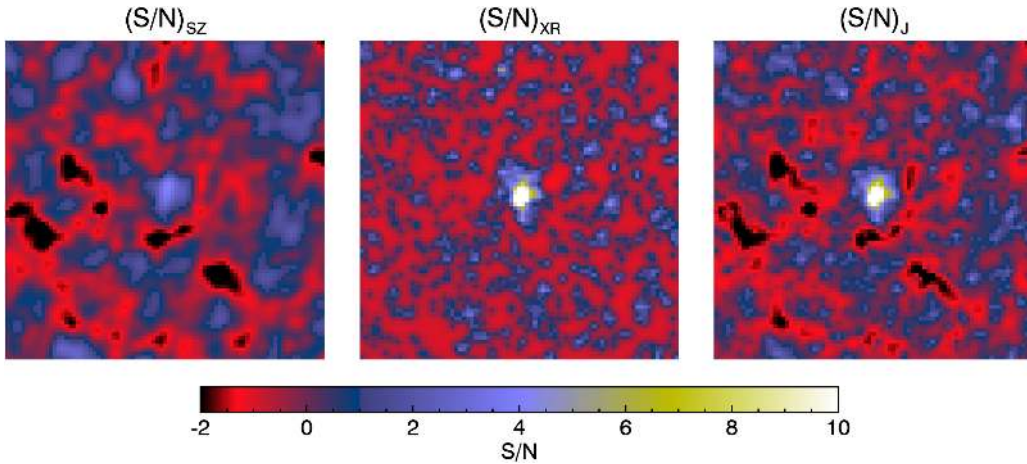
Fig. 12. S/N maps for the joint detection that matches RXC J0211.4-4017, a MCXC cluster not detected by *Planck* or SPT situated at $z = 0.1$ with $M_{500} = 1.65 \times 10^{14} \, M_\odot$. The three colour images show the S/N corresponding to the SZ filtered maps (*left*), the X-ray filtered map (*middle*) and the joint filtered maps (*right*). The filter size is 0.8 arcmin, which corresponds to the one that provides the best S/N for this detection. The angular size of the images is 68.7 arcmin. The RASS exposure time at the position of the detection is 946 s.

4.6. New candidates

As mentioned before, 193 of the 225 detections corresponding to $P_{FA} = 3.40 \times 10^{-6}$ match with a real cluster within a distance of 10 arcmin. This means that our catalogue contains 32 candidates that are not known clusters. They could be either false detections due to noise or to X-ray point sources, or true clusters not detected before. Table 5 summarizes the coordinates and some additional information of these 32 new candidates.

Since we set a false alarm probability of $P_{FA} = 3.40 \times 10^{-6}$ to calculate the joint S/N threshold, we expect to have 1.7 pixels in each filtered patch with $(S/N)_J$ greater than the threshold. This means that in the whole SPT area we expect to have 42 pixels above the threshold, producing at most 42 false detections due to noise fluctuations. This number is close to the number of new candidates, so can we expect most of them to be false detections. On the other hand, for $P_{FA} = 2.04 \times 10^{-7}$ and $P_{FA} = 1.90 \times 10^{-8}$ we would expect at most 2.5 and 0.2 false detections due to noise fluctuations in the SPT footprint, respectively. However, the number of new candidates for these two false alarm probabilities is 14 and 10, respectively (see Table 4). We expect then

that most of these candidates are real detections (either clusters or other objects like X-ray point sources). We indicate in Table 5 which of the 32 candidates corresponding to $P_{FA} = 3.40 \times 10^{-6}$ are also candidates for $P_{FA} = 2.04 \times 10^{-7}$ and $P_{FA} = 1.90 \times 10^{-8}$.

We searched for archival X-ray observations covering these 32 positions. Three of the candidates (1, 8, and 12) were observed by *Swift* (Burrows et al. 2005) and two more (14 and 32) by XMM-Newton. In the three *Swift* observations, there is evidence that the candidates are real clusters, since we can see an extended emission, as shown in Fig. 15. On the contrary, the two XMM-Newton observations show that the candidates are false detections: candidate 14 is a point source, while candidate 32 is just a noise fluctuation. As shown in the Table 5, the joint S/N of candidate 32 is just above the threshold.

We also looked around these 32 positions for other known galaxy clusters or groups in the NED[6] and SIMBAD[7] databases. Table 6 shows all the clusters and groups found closer than 10 arcmin to our candidates. Most of the joint candidates do not

---

[6] http://nedwww.ipac.caltech.edu/
[7] http://simbad.u-strasbg.fr/simbad
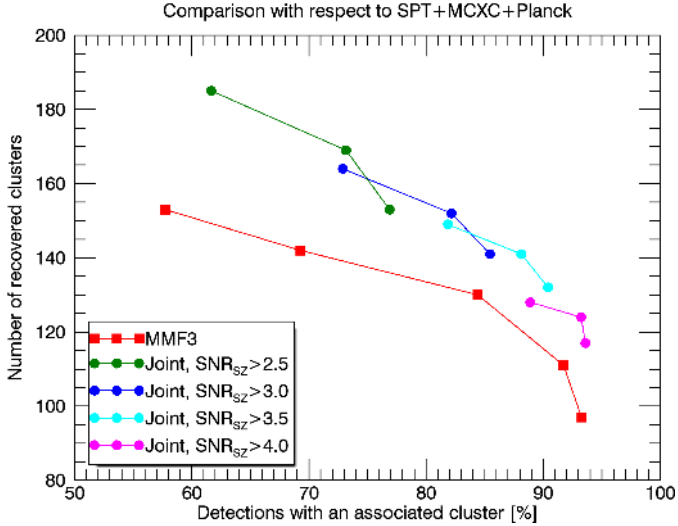
Fig. 13. Comparison of the performance of the proposed method (green, blue, cyan, and magenta circles) and the MMF3 method (red squares). The horizontal axis shows the percentage of detections which match a real cluster within a 10 arcmin radius. It is an indicator of the purity of the methods. The vertical axis shows the number of real clusters detected (which match a detection within a 10 arcmin radius). It is related to the detection efficiency of the methods. We assume that the real clusters in the considered region are all the clusters from the SPT, MCXC, and *Planck* catalogues with known mass and redshift (confirmed). The different points in the curves correspond to different operational points of the detection algorithms. For the MMF3 case we have represented the results for S/N thresholds of 4.00, 4.25, 4.50, 4.75, and 5.00, increasing from left to right. For the proposed algorithm, we have represented the results for $P_{FA} = 3.40 \times 10^{-6}$, $P_{FA} = 2.04 \times 10^{-7}$ and $P_{FA} = 1.90 \times 10^{-8}$, decreasing from left to right for each $(S/N)_{SZ}$ cut.
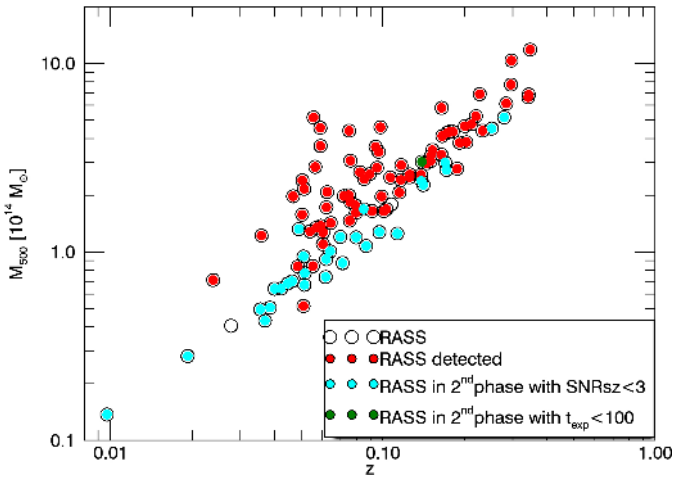

Fig. 14. Mass and redshift of the clusters in the RASS catalogue. Open circles represent RASS clusters in the considered region; red filled circles represent RASS clusters that are detected by the joint detection algorithm; cyan filled circles represent RASS clusters that were detected in the second phase of the algorithm, but discarded due to a low $(S/N)_{SZ}$; and the green-filled circle represents the RASS cluster that was detected in the second phase of the algorithm, but discarded due to a low exposure time.

have any NED or SIMBAD clusters close to them. For 13 candidates, we found some close-by objects, but in most of the cases, they do not seem to be associated with the candidate since their

separation is too big. Only candidates 12 and 21 might be associated with clusters: the SPT cluster SPT-CL J0438-4907 and the optical cluster LCS-CL J051723-5325.5, respectively.

We clarify that we did not match candidate 12 with SPT-CL J0438-4907 before (Sect. 4.1) because this cluster is not included in the published SPT catalogue of Bleem et al. (2015b) since its significance is lower than 4.5, which was the limit for the published catalogue. However, it is detected at lower significance and confirmed with optical observations in Saro et al. (2015). The presence of this cluster at only 0.7 arcmin from candidate 12 and the *Swift* observation presented in Fig. 15c are strong indicators that this candidate is a real cluster. Moreover, the mass obtained from the joint extraction assuming the redshift of the SPT cluster is $M_{500} = 3.04 \times 10^{14}\ M_\odot$, very close to the mass published by Saro et al. (2015) for the SPT cluster ($M_{500} = (3.13 \pm 0.81) \times 10^{14}\ M_\odot$).

Regarding candidate 21, the estimated mass assuming the redshift of the nearby optical cluster is $M_{500} = 3.38 \times 10^{14}\ M_\odot$. If we apply the richness-mass relation of Rozo et al. (2015), we get an estimated richness of $\lambda_e = 63.5$. According to Bleem et al. (2015a), the optical cluster LCS-CL J051723-5325.5 has a richness of $\lambda = 29.2$, which differs from λ_e by 2.92 $\sigma_{\ln\lambda}$. Given the large scatter of the richness-mass relation, it is reasonable to associate candidate 21 with cluster LCS-CL J051723-5325.5.

5. Conclusions

In this paper we have proposed a galaxy cluster detection method based on matched multifrequency filters (MMF) that combines X-ray and SZ observations. This method builds on the previously proposed joint X-ray–SZ extraction method and allows us to blindly detect clusters, i.e. finding new clusters without knowing their position, size, or redshift, by searching on SZ and X-ray maps simultaneously. It can be seen as an evolution of the MMF3 detection method, one of the MMF methods used to detect clusters from *Planck* observations, that incorporates X-ray observations to improve the detection performance.

The main challenge to solve was to obtain a high purity, since the addition of the X-ray information increases the cluster detection probability, but also the number of false detections, produced by AGNs and Poisson noise. To deal with the Poisson noise correctly, we proposed an adaptive S/N threshold to keep or discard detections depending on the noise characteristics of the region. To discard AGN detections, we proposed an additional classification according to the SZ part of the S/N.

The proposed method is tested using data from the RASS and *Planck* surveys and evaluated by comparing the detection results with existing cluster catalogues in the area of the sky covered by the SPT survey. We have shown that, thanks to the addition of the X-ray information, the method is able to simultaneously achieve better purity, better detection efficiency, and better position accuracy than its predecessor, the MMF3 detection method.

We have also shown that if the redshift of a cluster is known by any other means, the joint detection allows a good estimation of its mass. Some bias may appear in the presence of a cool core (overestimated mass) or if there is an offset between the X-ray and SZ peaks (underestimated mass).

Finally, we have produced a catalogue of candidates in the SPT region composed of 225 objects, with 32 new objects that are not included in other SZ or X-ray cluster catalogues. We have found, using *Swift* observations, that three of these new

Table 5. List of candidates for $P_{FA} = 3.40 \times 10^{-6}$ that do not match known clusters or cluster candidates, ordered by significance.

Id.	G. lon. [°]	G. lat. [°]	RA J2000 [°]	Dec J2000 [°]	$(S/N)_J$	$(S/N)_{SZ}$	q_J	$(S/N)_J$-q_J	Significance	Notes
1	262.127	−30.865	86.910	−54.310	13.72	3.28	4.70	9.02	10.62	**
2	272.610	−28.890	91.930	−63.244	9.46	4.23	4.87	4.59	7.62	**
3	356.016	−51.958	330.063	−43.514	9.05	3.08	6.00	3.04	6.57	**
4	269.926	−33.562	81.955	−60.928	7.70	4.06	4.84	2.86	6.44	**
5	266.726	−34.077	81.239	−58.245	7.58	3.23	4.92	2.65	6.30	**
6	299.961	−53.485	16.829	−63.551	7.45	3.04	5.15	2.30	6.06	**
7	282.665	−54.841	35.371	−58.601	6.77	3.94	4.77	2.00	5.75	**
8	265.689	−27.575	93.313	−57.045	7.12	3.48	4.71	2.42	5.67	**
9	270.400	−44.745	60.078	−58.641	6.93	3.01	5.00	1.93	5.65	**
10	254.861	−20.784	100.312	−45.874	6.20	3.74	4.84	1.36	5.47	**
11	327.280	−75.170	4.893	−40.415	7.36	4.03	5.54	1.82	5.43	**
12	255.846	−41.583	69.662	−49.106	5.56	3.58	4.53	1.02	5.35	*
13	346.731	−57.456	339.853	−46.882	9.40	3.52	6.77	2.63	5.26	**
14	290.504	−71.045	18.586	−45.527	7.07	3.02	5.64	1.43	5.25	*
15	249.394	−34.217	80.293	−43.930	5.58	3.56	4.84	0.74	5.19	*
16	357.238	−34.672	306.147	−43.350	5.79	3.51	4.87	0.91	5.14	*
17	283.847	−65.365	25.079	−49.914	6.65	3.52	5.86	0.79	4.93	
18	0.622	−48.152	324.445	−41.074	6.72	3.11	5.98	0.74	4.89	
19	352.487	−33.184	303.471	−47.119	5.69	3.73	5.14	0.55	4.86	
20	335.748	−37.097	310.996	−60.647	5.56	3.36	5.03	0.53	4.84	
21	260.921	−35.301	79.333	−53.436	5.54	3.03	4.98	0.57	4.84	
22	265.024	−30.437	87.988	−56.765	5.11	3.45	4.74	0.37	4.74	
23	356.548	−41.337	315.336	−44.232	4.89	3.84	4.69	0.20	4.70	
24	277.913	−65.311	28.381	−48.691	5.34	3.97	5.06	0.28	4.68	
25	274.955	−58.096	37.411	−53.368	5.72	3.12	5.43	0.29	4.65	
26	282.535	−53.687	36.837	−59.477	5.34	3.13	5.16	0.18	4.62	
27	258.667	−34.133	81.229	−51.574	4.98	3.45	4.85	0.13	4.58	
28	260.348	−20.324	103.375	−50.613	4.94	4.43	4.87	0.07	4.53	
29	252.269	−23.928	95.065	−44.475	4.96	3.64	4.88	0.08	4.53	
30	264.135	−35.097	79.543	−56.066	4.63	3.41	4.61	0.03	4.51	
31	254.233	−25.041	94.169	−46.485	4.84	3.19	4.82	0.01	4.51	
32	328.390	−59.170	351.147	−53.453	5.77	3.46	5.65	0.13	4.43	

Notes. Galactic and equatorial coordinates are given in degrees. The joint S/N is indicated, as well as the SZ component of this S/N. Finally, the joint threshold q_J, the difference between the S/N and the threshold, and the significance are shown. The last column indicates whether the candidate is also a candidate for $P_{FA} = 2.04 \times 10^{-7}$ and $P_{FA} = 1.90 \times 10^{-8}$ (* indicates that it is also a candidate for $P_{FA} = 2.04 \times 10^{-7}$, ** indicates that it is a candidate for both $P_{FA} = 2.04 \times 10^{-7}$ and $P_{FA} = 1.90 \times 10^{-8}$).

(a)	(b)	(c)
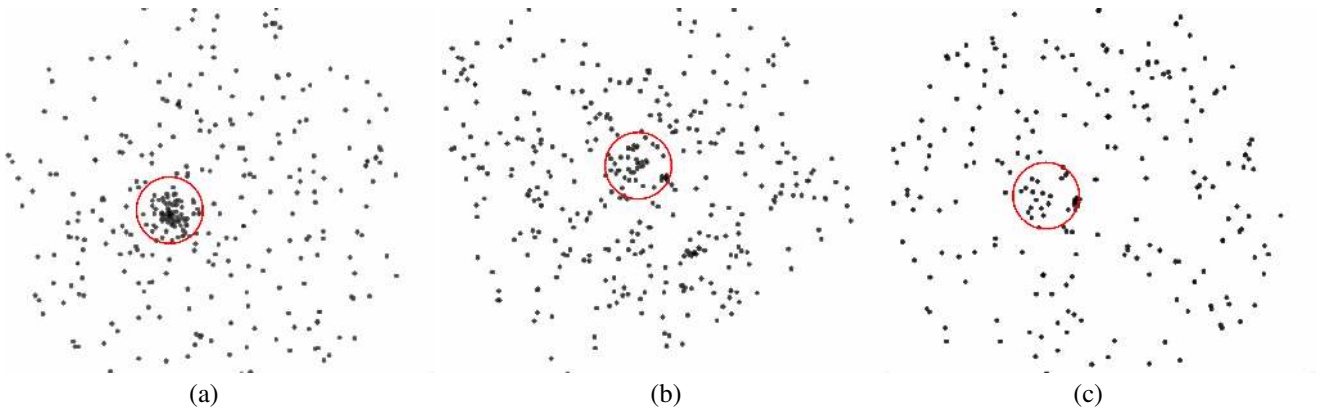
Fig. 15. *Swift* observations of candidates 1 (*a*), 8 (*b*), and 12 (*c*). A red circle with 2 arcmin radius centred at the candidate position was added for visual reference.

Table 6. Galaxy clusters and galaxy groups found close to the 32 candidates listed in Table 5.

Id.	Name	Type	Redshift	Separation [arcmin]
1	Str 0547-543	Cluster		3.2
3	NGC 7166	Group	0.0077	7.1
	[CHM2007] HDC 1172	Group		4.6
	LGG 449	Group		7.1
	NOGG H 1003	Group		7.5
7	[LH2011] 3692	Group		7.0
11	[RZZ99] ESP 121	Group		5.0
	Str 0018-407	Cluster		5.0
	EDCC 435	Cluster	0.15	8.6
12	SPT-CL J0438-4907	Cluster	0.24	0.7
14	LCLG -45 038	Group	0.0897	7.6
18	APMCC 688	Group	0.065	3.6
	LCLG -42 164	Group	0.065	9.2
20	APM CC 607	Cluster		2.3
	Str 2040-608	Cluster		2.8
21	LCS-CL J051723-5325.5	Cluster	0.37	0.8
	LCS-CL J051759-5326.4	Cluster	0.39	5.9
	LCS-CL J051813-5327.2	Cluster	0.62	8.0
23	APMCC 621	Cluster	0.143	4.9
	[DEM94] 205740.8-442233	Cluster		5.8
	QW 146	Cluster		6.8
27	LCS-CL J052516-5134.1	Cluster	0.22	3.3
	LCS-CL J052502-5134.1	Cluster	0.24	9.8
30	SCSO J051755-555727	Cluster	0.66	6.9
32	SCSO J232529-532420	Cluster	0.74	8.5

Notes. The search was done in the NED and SIMBAD databases.

objects are probably real clusters. This supports the fact that the proposed method can be used to find new clusters.

In future work we will run the joint detection on all the sky using *Planck* and RASS maps and we will provide the last and deepest all-sky cluster catalogue before the e-ROSITA mission.

References

Abell, G. O., Corwin, Jr. H. G., & Olowin, R. P. 1989, ApJS, 70, 1
Arnaud, M., Pratt, G. W., Piffaretti, R., et al. 2010, A&A, 517, A92
Bleem, L. E., Stalder, B., Brodwin, M., et al. 2015a, ApJS, 216, 20
Bleem, L. E., Stalder, B., de Haan, T., et al. 2015b, ApJS, 216, 27
Böhringer, H., Voges, W., Huchra, J. P., et al. 2000, ApJS, 129, 435
Böhringer, H., Schuecker, P., Guzzo, L., et al. 2001, A&A, 369, 826
Böhringer, H., Chon, G., Collins, C. A., et al. 2013, A&A, 555, A30
Burrows, D. N., Hill, J. E., Nousek, J. A., et al. 2005, Space Sci. Rev., 120, 165
Delabrouille, J., Betoule, M., Melin, J.-B., et al. 2013, A&A, 553, A96
Ebeling, H. & Wiedenmann, G. 1993, Phys. Rev. E, 47, 704
Ebeling, H., Edge, A. C., & Henry, J. P. 2001, ApJ, 553, 668
Górski, K. M., Hivon, E., Banday, A. J., et al. 2005, ApJ, 622, 759
Hasselfield, M., Hilton, M., Marriage, T. A., et al. 2013, JCAP, 7, 8
Herranz, D., Sanz, J. L., Hobson, M. P., et al. 2002, MNRAS, 336, 1057
Hudson, D. S., Mittal, R., Reiprich, T. H., et al. 2010, A&A, 513, A37
Maturi, M. 2007, Astron. Nachr., 328, 690
Melin, J.-B., Bartlett, J. G., & Delabrouille, J. 2006, A&A, 459, 341
Melin, J.-B., Aghanim, N., Bartelmann, M., et al. 2012, A&A, 548, A51
Merloni, A., Predehl, P., Becker, W., et al. 2012, ArXiv e-prints [arXiv:1209.3114]
Nagai, D., Kravtsov, A. V., & Vikhlinin, A. 2007, ApJ, 668, 1
Pacaud, F., Pierre, M., Refregier, A., et al. 2006, MNRAS, 372, 578
Pace, F., Maturi, M., Bartelmann, M., et al. 2008, A&A, 483, 389
Piffaretti, R., Arnaud, M., Pratt, G. W., Pointecouteau, E., & Melin, J.-B. 2011, A&A, 534, A109
Planck Collaboration VIII. 2011, A&A, 536, A8
Planck Collaboration XX. 2014, A&A, 571, A20
Planck Collaboration XXIX. 2014, A&A, 571, A29
Planck Collaboration VIII. 2016, A&A, 594, A8
Planck Collaboration XXVI. 2016, A&A, 594, A26
Planck Collaboration XXVII. 2016, A&A, 594, A27
Planck Collaboration Int. I. 2012, A&A, 543, A102
Rozo, E., Rykoff, E. S., Bartlett, J. G., & Melin, J.-B. 2015, MNRAS, 450, 592
Saro, A., Bocquet, S., Rozo, E., et al. 2015, MNRAS, 454, 2305
Scharf, C. A., Ebeling, H., Perlman, E., Malkan, M., & Wegner, G. 1997, ApJ, 477, 79
Schuecker, P., Böhringer, H., & Voges, W. 2004, A&A, 420, 61
Sunyaev, R. A., & Zeldovich, Y. B. 1970, Comm. Astrophys. Space Phys., 2, 66
Sunyaev, R. A., & Zeldovich, Y. B. 1972, Comm. Astrophys. Space Phys., 4, 173
Tarrío, P., Melin, J.-B., Arnaud, M., & Pratt, G. W. 2016, A&A, 591, A39
Truemper, J. 1993, Science, 260, 1769
Vikhlinin, A., McNamara, B. R., Forman, W., et al. 1998, ApJ, 502, 558
Voges, W., Aschenbach, B., Boller, T., et al. 1999, A&A, 349, 389
York, D. G., Adelman, J., Anderson, Jr. J. E., et al. 2000, AJ, 120, 1579

Appendix A: Matching of simulation results with real maps parameters

As explained in Sect. 3.3, the X-ray noise maps used in the Monte Carlo simulations were simulated as homogeneous Poisson random fields, characterized by a given mean value λ (in counts). To express these count maps in $\Delta T/T$ units, as was done with real RASS count maps, we need to assume an exposure time map and a N_H map, and then apply the conversion procedure described in Appendix B of Tarrío et al. (2016), which can be summarized as follows:

$$M[\Delta T/T] = \frac{M[\text{counts}]}{t_{\text{exp}}[\text{s}]} \cdot c(N_H) \cdot \left[\frac{F_X}{Y_{500}}\right]^{-1}_{z_{\text{ref}}} \cdot \frac{g(\nu_{\text{ref}})}{d^2_{\text{pix}}}. \tag{A.1}$$

In this expression $c(N_H)$ represents the factor that converts the count rate into X-ray flux and it depends on the N_H map; the expected F_X/Y_{500} relation is used to convert the X-ray flux into equivalent Y_{500} integrated flux and depends on the reference redshift; d^2_{pix} is the HEALPix pixel area and $g(\nu_{\text{ref}})$ is the factor that converts from y units into $\Delta T/T_{\text{CMB}}$ units, which depends on the reference frequency assumed for the map (1000 GHz in our case).

For the Monte Carlo simulations of this paper, we assumed a constant exposure time $t_{\text{exp}} = 400$ s and a constant $N_H = 2 \times 10^{20}$ cm^{-2} (average values in the SPT region). If other values were used, the resulting X-ray maps in $\Delta T/T$ units would only differ from the ones obtained with these values by a constant factor a. This allows us to convert some of the simulation results obtained for the reference t_{exp} and N_H values (in particular $\sigma^x_{\theta_s}$ and S/N) into the results corresponding to any other value of t_{exp} and/or N_H. In the following, we explain how this conversion is done.

Let M_x and M'_x be two X-ray maps in $\Delta T/T$ units, calculated from the same count map using different values of t_{exp} and N_H. From Eq. (A.1), we have the following relation between the two maps:

$$M'_x = \frac{M_x}{a}, \tag{A.2}$$

where

$$a = \frac{t'_{\text{exp}}}{t_{\text{exp}}} \cdot \frac{c(N_H)}{c(N'_H)}. \tag{A.3}$$

Let $\mathbf{M} = [\mathbf{N}_{\text{sz}}, N_x]^T$ and $\mathbf{M}' = [\mathbf{N}_{\text{sz}}, N'_x]^T = [\mathbf{N}_{\text{sz}}, N_x/a]^T$ be two multifrequency noise maps whose SZ components are equal and whose X-ray components differ by a constant factor a.

Considering that the noise in the X-ray map and the SZ maps is uncorrelated, we can write the noise power spectrum of $\mathbf{M}$ as

$$\mathbf{P} = \begin{bmatrix} \mathbf{P}_{\text{sz}} & \mathbf{0}_{N_\nu \times 1} \\ \mathbf{0}_{1 \times N_\nu} & P_x \end{bmatrix}, \tag{A.4}$$

where $\mathbf{P}_{\text{sz}}$ is the noise power spectrum of the SZ maps $\mathbf{N}_{\text{sz}}$, P_x is the noise power spectrum of the X-ray map N_x, and $\mathbf{0}_{n \times m}$ denotes a vector with n rows and m columns whose elements are all equal to 0. The noise power spectrum of $\mathbf{M}'$ can be decomposed into $\mathbf{P}_{\text{sz}}$ and P'_x in an analogous way. Using the definition of the noise power spectrum (see Sect. 3.1), it is immediate to show that $P'_x = a^{-2}P_x$.

Using the definition of the variance of the filtered maps (Eq. (2)) and applying (A.4), we can also decompose the variance of the filtered maps into an SZ and an X-ray component as

$$\sigma^{-2}_{\theta_s} = \mathbf{F}^T_{\text{sz}}\mathbf{P}^{-1}_{\text{sz}}\mathbf{F}_{\text{sz}} + F^T_x P^{-1}_x F_x = \sigma^{-2}_{\text{sz}} + \sigma^{-2}_x, \tag{A.5}$$

where $\mathbf{F}_{\text{sz}}$ and F_x are the SZ and X-ray components of $\mathbf{F}_{\theta_s}$ (Eq. (3)). From this expression it is easy to show that

$$\sigma'_x = \frac{\sigma_x}{a}. \tag{A.6}$$

If we filter $\mathbf{M}$ and $\mathbf{M}'$ with the proposed joint filter (Eq. (1)), the S/N of the filtered maps will be given by

$$\text{S/N} = \sigma_{\theta_s}\left[\mathbf{F}^*_{\text{sz}}\mathbf{P}^{*-1}_{\text{sz}}\mathbf{N}_{\text{sz}} + F^*_x P^{*-1}_x N_x\right] \tag{A.7}$$

and

$$\text{S/N}' = \sigma'_{\theta_s}\left[\mathbf{F}^*_{\text{sz}}\mathbf{P}^{*-1}_{\text{sz}}\mathbf{N}_{\text{sz}} + aF^*_x P^{*-1}_x N_x\right]. \tag{A.8}$$

From these two expressions, and taking into account (A.5) and (A.6), we can obtain the relation between the S/N of the two noise maps as

$$\text{S/N}' = \text{S/N} \cdot \sqrt{\frac{1+\omega}{1+a^2\omega}} \cdot \frac{1+aW}{1+W}, \tag{A.9}$$

where

$$\omega = \left(\frac{\sigma_{\text{sz}}}{\sigma_x}\right)^2 \tag{A.10}$$

and

$$W = \frac{F^*_x P^{*-1}_x N_x}{\mathbf{F}^*_{\text{sz}}\mathbf{P}^{*-1}_{\text{sz}}\mathbf{N}_{\text{sz}}}. \tag{A.11}$$

Appendix B: Significance estimation

As explained in Sect. 3.5, the significance of a detection is calculated with the aid of the S/N maps obtained from the numerical simulations described in Sect. 3.3. In particular, it is obtained by measuring the number of pixels in the simulations that have a S/N higher than the S/N of the detection. Given that the number of simulated pixels is finite, when the joint S/N of the detection is very high, there may be no pixels satisfying this condition. In these cases, it is not possible to calculate the significance directly. Since for each combination of mean Poisson level λ and mean Gaussian level σ_{217} we created 450 random realizations of the noise maps, and since each map has 700×700 pixels, the minimum false alarm probability that we can determine is 4.5×10^{-9}. This means that when we do not find any pixels above a given S/N, we can only affirm that the significance will be higher than 5.75.

To find a way to estimate the significance in these cases, we analysed the second phase detections corresponding to $P_{\text{FA}} = 3.40 \times 10^{-6}$. We calculated the significance of the detections with $(S/N)_{\text{SZ}} > 3$ outside the SZ mask and we found a good correlation between the significance and the difference between the joint S/N and the threshold q_J, as shown in Fig. B.1. Therefore, we decided to use a linear extrapolation to estimate the values of significance as a function of $(S/N)_J - q_J$ for the detections whose calculated significance is >5.75. By definition, the significance
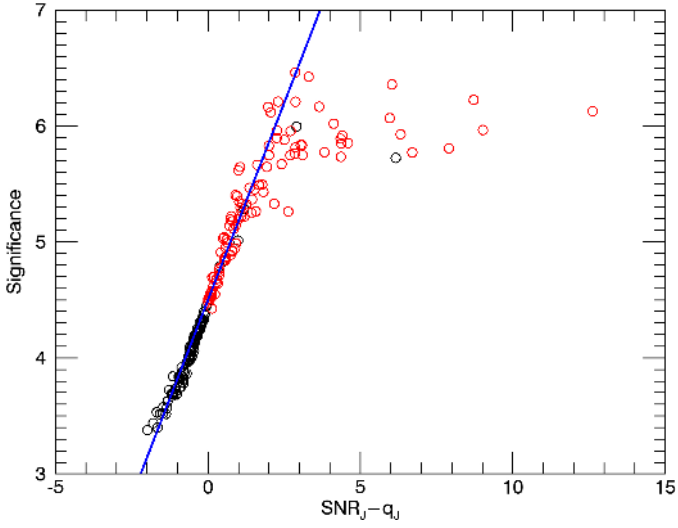
Fig. B.1. Significance as a function of $(S/N)_J - q_J$ for the second phase detections corresponding to $P_{FA} = 3.40 \times 10^{-6}$, with $(S/N)_{SZ} > 3$ and outside the SZ mask. Red circles indicate the detections that pass all the other cuts ($t_{exp} > 100$ s and $(S/N)_J > q_J$), while black circles indicate the detections that do not pass them. The solid blue line is the best linear fit with a fixed intercept of 4.5.

corresponding to $(S/N)_J = q_J$ is 4.5 for $P_{FA} = 3.40 \times 10^{-6}$. Thus, the linear extrapolation was found by fitting a line with a fixed intercept of 4.5 to the points in Fig. B.1, excluding the outliers. The final expression we obtained is

$$\text{significance} = 4.5 + 0.68 \cdot ((S/N)_J - q_J). \tag{B.1}$$

Appendix C: List of candidates

Table C.1. List of candidates for $P_{FA} = 3.40 \times 10^{-6}$, ordered according to their significance.

Id.	G. lon. [°]	G. lat. [°]	RA J2000 [°]	Dec J2000 [°]	$(S/N)_J$	$(S/N)_{SZ}$	q_J	$(S/N)_J - q_J$	Significance	PSZ2	SPT	MCXC	Abell	z	M_{500} [$10^{14} M_\odot$]
1	252.918	−56.071	49.505	−44.232	124.37	9.77	5.13	119.24	85.47	PSZ2 G252.99-56.09		RXC J0317.9-4414	ABELL 3112	0.08	6.89
2	272.108	−40.136	67.857	−61.429	92.35	32.68	4.58	87.77	64.10	PSZ2 G272.08-40.16	SPT-CLJ0431-6126	RXC J0431.4-6126	ABELL 3266	0.06	4.86
3	265.042	−48.932	55.733	−53.630	83.91	17.71	4.73	79.18	58.27	PSZ2 G265.02-48.96		RXC J0342.8-5338	ABELL 3158	0.06	4.43
4	348.350	−64.811	348.488	−42.727	66.96	3.74	5.15	61.81	46.47	PSZ2 G348.46-64.83	SPT-CLJ2313-4243	RXC J2313.9-4244	ACOS 1101	0.06	4.78
5	340.852	−33.392	303.128	−56.840	55.74	21.76	4.65	51.09	39.20	PSZ2 G340.88-33.36	SPT-CLJ2012-5649	RXC J2012.5-5649	ABELL 3667	0.06	4.97
6	349.492	−59.929	342.173	−44.527	55.29	21.36	5.51	49.78	38.30	PSZ2 G349.46-59.95	SPT-CLJ2248-4431	RXC J2248.7-4431	ACOS 1063	0.35	14.52
7	332.212	−46.369	330.472	−59.961	51.71	19.52	4.78	46.92	36.36	PSZ2 G332.23-46.37	SPT-CLJ2201-5956	RXC J2201.9-5956	ABELL 3827	0.10	5.67
8	266.038	−21.238	104.652	−55.956	48.79	28.65	4.98	43.81	34.25	PSZ2 G266.04-21.25	SPT-CLJ0658-5556	RXC J0658.5-5556		0.30	12.46
9	263.681	−22.551	101.369	−54.229	46.11	22.82	4.91	41.19	32.47	PSZ2 G263.68-22.55	SPT-CLJ0645-5413	RXC J0645.4-5413	ABELL 3404	0.16	7.49
10	321.963	−47.975	342.492	−64.418	42.97	13.80	4.82	38.15	30.40	PSZ2 G321.98-47.96	SPT-CLJ2249-6426	RXC J2249.9-6425	ABELL 3921	0.09	4.59
11	271.197	−30.970	87.315	−62.087	40.24	14.30	4.93	35.31	28.48	PSZ2 G271.18-30.95	SPT-CLJ0549-6205			0.37	7.50
12	246.413	−30.288	85.030	−40.838	39.70	4.43	4.79	34.91	28.20	PSZ2 G246.36-30.27		RXC J0540.1-4050	ACOS 540	0.04	1.86
13	263.130	−23.428	99.699	−53.966	39.12	13.50	4.75	34.37	27.84	PSZ2 G263.14-23.41	SPT-CLJ0638-5358	RXC J0638.7-5358	ACOS 592	0.23	8.61
14	335.592	−46.464	328.547	−57.851	36.98	13.24	4.81	32.17	26.35	PSZ2 G335.58-46.44		RXC J2154.1-5751	ABELL 3822	0.08	3.61
15	270.988	−31.757	85.642	−61.902	35.85	4.57	4.90	30.95	25.51	PSZ2 G270.95-31.78				0.14	2.28
16	269.311	−49.893	52.142	−55.710	35.12	9.63	4.88	30.24	25.03	PSZ2 G269.31-49.87	SPT-CLJ0328-5541	RXC J0328.6-5542	ABELL 3126	0.09	3.46
17	336.594	−55.435	341.577	−52.727	33.57	13.74	4.96	28.62	23.93	PSZ2 G336.60-55.43		RXC J2246.3-5243	ABELL 3911	0.10	3.66
18	249.887	−21.650	97.204	−41.723	33.44	5.97	4.89	28.55	23.89	PSZ2 G249.87-21.65	SPT-CLJ0628-4143	RXC J0628.8-4143	ABELL 3396	0.18	6.58
19	262.372	−25.143	96.602	−53.690	31.42	10.38	4.60	26.82	22.71	PSZ2 G262.36-25.15		RXC J0626.3-5341	ABELL 3391	0.05	2.41
20	259.969	−63.445	38.079	−44.350	32.04	12.57	5.26	26.78	22.68	PSZ2 G259.98-63.43	SPT-CLJ0232-4421	RXC J0232.2-4420		0.28	7.82
21	255.316	−56.290	48.595	−45.420	31.59	4.60	5.19	26.40	22.43	PSZ2 G255.32-56.27		RXC J0314.3-4525	ABELL 3104	0.07	2.62
22	256.487	−65.712	36.470	−41.903	29.49	11.21	5.24	24.26	20.97	PSZ2 G256.53-65.70	SPT-CLJ0225-4155	RXC J0225.9-4154	ABELL 3017	0.22	6.33
23	262.254	−35.383	79.148	−54.520	28.33	24.13	4.88	23.45	20.42	PSZ2 G262.27-35.38	SPT-CLJ0516-5430	RXC J0516.6-5430	ACOS 520	0.30	7.42
24	337.997	−45.692	326.009	−56.630	28.13	3.30	5.03	23.10	20.19			RXC J2143.9-5637		0.08	3.62
25	246.506	−26.043	90.489	−39.971	24.82	10.53	4.56	20.26	18.26	PSZ2 G246.50-26.09		RXC J0601.7-3959		0.05	1.70
26	273.539	−30.283	88.852	−64.099	24.30	7.92	4.93	19.37	17.65	PSZ2 G273.54-30.28	SPT-CLJ0555-6406			0.35	5.79
27	264.820	−51.135	52.478	−52.602	23.44	7.39	4.72	18.72	17.21	PSZ2 G264.60-51.07	SPT-CLJ0330-5228	RXC J0330.0-5235	ABELL 3128	0.44	7.47
28	356.079	−49.531	326.747	−43.895	23.48	4.51	4.96	18.52	17.08	PSZ2 G356.04-49.50			ABELL 3809	0.06	1.90
29	263.289	−25.265	96.695	−54.527	22.63	9.68	4.55	18.08	16.77	PSZ2 G263.19-25.19		RXC J0627.2-5428		0.05	2.02
30	271.527	−56.581	41.363	−53.030	23.04	11.17	5.02	18.02	16.73	PSZ2 G271.53-56.57			ACOS 295	0.30	7.27
31	272.091	−29.042	91.534	−62.800	22.41	6.21	4.71	17.69	16.52	PSZ2 G272.08-29.06			ACOS 567	0.10	2.19
32	285.508	−62.255	26.260	−53.022	22.41	9.13	4.97	17.43	16.34	PSZ2 G285.52-62.23	SPT-CLJ0145-5301	RXC J0145.0-5300	ABELL 2941	0.12	3.46
33	249.914	−39.851	72.466	−44.685	22.51	7.71	5.09	17.42	16.33	PSZ2 G249.91-39.86		RXC J0449.9-4440	ABELL 3292	0.15	4.39
34	324.518	−44.971	334.513	−65.195	21.12	8.47	4.62	16.50	15.70	PSZ2 G324.54-44.97	SPT-CLJ2217-6509	RXC J2218.0-6511		0.10	3.56
35	250.889	−36.270	77.568	−45.324	20.94	12.43	4.95	15.99	15.36	PSZ2 G250.89-36.24	SPT-CLJ0510-4519	RXC J0510.2-4519	ABELL 3322	0.20	5.15
36	274.753	−32.179	84.354	−65.072	20.59	4.58	5.03	15.56	15.07	PSZ2 G274.73-32.20	SPT-CLJ0537-6504			0.20	3.23
37	250.720	−30.352	85.851	−44.508	20.22	3.08	4.79	15.44	14.98			RXC J0543.4-4430		0.16	4.29
38	247.159	−23.314	94.123	−39.806	20.18	8.21	4.78	15.40	14.95	PSZ2 G247.19-23.31		RXC J0616.5-3948	ACOS 579	0.15	4.14
39	253.480	−33.724	81.467	−47.254	20.20	9.44	4.82	15.39	14.95	PSZ2 G253.48-33.72	SPT-CLJ0525-4715	RXC J0525.8-4715	ABELL 3343	0.19	4.83
40	336.953	−45.747	326.608	−57.284	20.20	6.52	4.83	15.37	14.94	PSZ2 G336.95-45.75		RXC J2146.3-5717	ABELL 3806	0.08	2.50
41	322.634	−49.140	343.512	−63.256	20.35	7.86	4.99	15.36	14.93	PSZ2 G322.63-49.15	SPT-CLJ2254-6314	RXC J2254.0-6315		0.21	5.30
42	293.098	−70.858	17.477	−45.916	19.89	6.54	4.71	15.18	14.80	PSZ2 G293.12-70.85		RXC J0110.0-4555	ABELL 2877	0.02	0.91
43	277.729	−51.733	43.613	−58.952	20.23	15.04	5.09	15.14	14.78	PSZ2 G277.76-51.74	SPT-CLJ0254-5857			0.44	8.58
44	352.851	−49.322	326.976	−45.999	19.33	4.04	5.04	14.29	14.20			RXC J2147.9-4600	ACOS 974	0.06	1.62
45	0.403	−41.864	316.089	−41.354	19.08	9.61	4.79	14.28	14.20	PSZ2 G000.40-41.86		RXC J2104.3-4120	ABELL 3739	0.17	5.25
46	275.968	−41.473	62.877	−63.680	18.87	3.70	4.92	13.95	13.97		SPT-CLJ0411-6340		ABELL 3230	0.14	3.46
47	257.328	−22.198	99.324	−48.485	18.43	10.77	4.70	13.73	13.83	PSZ2 G257.32-22.19	SPT-CLJ0637-4829	RXC J0637.3-4828	ABELL 3399	0.20	4.72
48	348.315	−66.454	350.402	−41.892	18.62	3.19	4.98	13.64	13.76			RXC J2321.5-4153	ABELL 3998	0.09	3.21
49	339.612	−69.321	356.169	−42.739	18.34	8.83	5.49	12.84	13.22	PSZ2 G339.63-69.34	SPT-CLJ2344-4243			0.60	11.36
50	256.571	−68.894	32.834	−40.283	18.38	3.56	5.55	12.84	13.22			RXC J0211.4-4017	ABELL 2984	0.10	2.31

Notes. Galactic and equatorial coordinates are given in degrees in Cols. 2–5. Column 6 indicates the joint S/N, while Col. 7 shows the SZ component of this S/N. The joint threshold q_J and the difference between the S/N and the threshold are shown in Cols. 8 and 9. Column 10 indicates the significance, calculated as explained in Sect. 4. Columns 11–14 show the names of the objects from the PSZ2, SPT, MCXC, and Abell catalogues that match our candidates. Column 15 indicates the redshift of the matching cluster, if it is available (if several are available, we preferentially show the SZ redshift, then the MCXC redshift, and finally the Abell redshift). The last column shows our mass estimation using the SZ redshift or the MCXC redshift (the former is shown if both are available).

Table C.1. continued.

Id	G. lon. [°]	G. lat. [°]	RA J2000 [°]	Dec J2000 [°]	$(S/N)_J$	$(S/N)_{SZ}$	q_J	$(S/N)_J \cdot q_J$	Significance	PSZ2	SPT	MCXC	Abell	z	M_{500} [$10^{14}\,M_\odot$]
51	245.675	−33.761	80.365	−40.813	17.40	5.53	4.77	12.62	13.07	PSZ2 G245.70-33.75		RXC J0521.4-4049	ABELL 3336	0.08	2.18
52	291.343	−55.329	26.309	−60.572	16.77	6.40	4.86	11.91	12.59	PSZ2 G291.34-55.31	SPT-CLJ0145-6033	RXC J0145.2-6033		0.18	4.58
53	278.217	−41.515	61.078	−65.175	16.66	5.76	4.92	11.75	12.48	PSZ2 G278.33-41.53	SPT-CLJ0404-6510	RXC J0404.6-6510	ABELL 3216	0.12	2.87
54	255.663	−25.317	94.221	−47.808	16.40	6.86	4.76	11.64	12.40	PSZ2 G255.64-25.30		RXC J0616.8-4748		0.12	2.89
55	298.024	−67.760	15.703	−49.259	17.15	12.71	5.56	11.59	12.37	PSZ2 G297.97-67.74	SPT-CLJ0102-4915			0.87	11.05
56	342.531	−50.944	332.329	−51.829	16.57	4.14	5.15	11.42	12.25	PSZ2 G342.51-50.97		RXC J2209.3-5148	ABELL 3836	0.11	2.48
57	345.825	−34.284	304.692	−52.711	16.05	4.21	4.70	11.35	12.21	PSZ2 G345.82-34.29		RXC J2018.7-5242	ACOS 861	0.05	2.01
58	245.487	−53.615	54.070	−40.631	16.25	8.23	4.90	11.34	12.20	PSZ2 G245.47-53.62		RXC J0336.3-4037	ABELL 3140	0.17	4.75
59	247.558	−56.069	50.582	−41.347	14.55	4.37	4.79	9.76	11.13	PSZ2 G247.56-56.06		RXC J0322.3-4121	ABELL 3122	0.06	1.60
60	336.016	−51.369	336.131	−55.260	14.56	4.05	4.94	9.62	11.03	PSZ2 G336.01-51.27		RXC J2224.5-5515		0.08	1.84
61	254.713	−30.502	86.388	−47.934	13.87	5.40	4.64	9.22	10.76	PSZ2 G254.73-30.52		RXC J0545.5-4756	ABELL 3363	0.13	2.38
62	262.127	−30.865	86.910		13.72	3.28	4.70	9.02	10.62	PSZ2 G262.13-30.87				0.42	7.07
63	262.730	−40.971	69.523	−54.310	14.46	10.10	5.45	9.01	10.62	PSZ2 G262.73-40.92	SPT-CLJ0438-5419		ABELL 2777	0.14	3.48
64	312.556	−66.427	6.857	−50.250	13.58	6.11	4.86	8.72	10.42	PSZ2 G312.63-66.40	SPT-CLJ0027-5015	RXC J0027.3-5015	ABELL 3825	0.08	1.90
65	331.971	−45.773	329.592	−60.398	13.36	5.37	4.69	8.66	10.38	PSZ2 G331.96-45.74		RXC J2158.4-6023	ABELL 3231	0.06	
66	277.045	−41.037	63.006	−64.598	13.76	4.07	5.10	8.66	10.38	PSZ2 G277.05-41.04				0.25	3.95
67	271.303	−36.123	76.374	−61.753	13.30	5.81	4.94	8.37	10.18	PSZ2 G271.28-36.11	SPT-CLJ0505-6145			0.15	3.59
68	359.072	−32.114	302.999	−41.483	13.21	7.04	4.90	8.30	10.14	PSZ2 G359.07-32.12	SPT-CLJ2012-4130	RXC J2012.0-4129	ABELL 3668	0.35	6.58
69	309.397	−72.852	10.208	−44.143	13.92	6.07	5.64	8.28	10.12	PSZ2 G309.43-72.86	SPT-CLJ0040-4407			0.34	6.53
70	0.757	−35.699	307.971	−40.613	13.11	6.50	4.92	8.19	10.06	PSZ2 G000.77-35.69	SPT-CLJ2031-4037	RXC J2031.8-4037		0.09	1.90
71	255.541	−35.698	78.659	−49.058	12.88	5.85	4.69	8.19	10.06	PSZ2 G255.52-35.66		RXC J0514.6-4903	ABELL 3330	0.41	6.56
72	280.272	−53.834	38.666	−58.516	13.56	5.95	5.47	8.09	9.99	PSZ2 G280.23-53.84	SPT-CLJ0234-5831			0.10	3.53
73	267.196	−34.967	79.498	−58.576	12.58	4.39	4.68	7.91	9.87	PSZ2 G267.20-34.97					
74	358.353	−47.312	323.476	−42.659	13.72	5.19	5.94	7.79	9.79	PSZ2 G358.34-47.31	SPT-CLJ2134-4238		ABELL 3334	0.20	5.14
75	276.802	−59.815	34.313	−52.741	12.70	5.11	5.03	7.67	9.71	PSZ2 G276.75-59.82	SPT-CLJ0217-5245	RXC J0217.2-5244	ABELL 3783	0.34	6.31
76	265.129	−59.508	40.895	−48.568	12.82	6.38	5.17	7.65	9.69	PSZ2 G265.10-59.50	SPT-CLJ0243-4833			0.50	5.38
77	270.660	−35.672	77.479	−61.308	12.82	8.01	5.23	7.59	9.65	PSZ2 G270.63-35.67	SPT-CLJ0509-6118			0.31	4.78
78	254.531	−27.306	91.021	−47.241	12.27	7.26	4.78	7.50	9.59	PSZ2 G254.51-27.32	SPT-CLJ0603-4714			0.27	5.22
79	342.335	−34.935	305.851	−55.577	12.11	9.15	4.87	7.24	9.42	PSZ2 G342.33-34.93	SPT-CLJ2023-5535	RXC J2023.4-5535		0.23	5.24
80	270.952	−58.797	38.928	−51.363	12.30	8.63	5.31	6.99	9.24	PSZ2 G270.93-58.78	SPT-CLJ0235-5121			0.28	6.72
81	1.844	−46.923	322.772	−40.310	12.88	4.51	5.97	6.92	9.20	PSZ2 G001.84-46.92	SPT-CLJ2131-4019			0.45	4.02
82	347.229	−52.463	332.847	−48.563	12.89	4.37	6.00	6.88	9.17	PSZ2 G347.27-52.46	SPT-CLJ2211-4833		ABELL 3841	0.24	7.10
83	348.940	−67.400	351.306	−41.187	12.66	7.68	5.83	6.83	9.14	PSZ2 G348.90-67.37	SPT-CLJ2325-4111		ACOS 1121	0.36	1.69
84	245.996	−51.753	56.451	−41.200	11.62	3.30	4.92	6.70	9.05	PSZ2 G246.01-51.76		RXC J0345.7-4112	ABELL 384	0.06	3.39
85	259.191	−19.122	104.589	−49.191	11.19	5.33	4.82	6.38	8.83	PSZ2 G259.19-19.12			ABELL 3406	0.16	6.34
86	255.625	−46.169	62.807	−48.319	11.08	9.28	4.76	6.32	8.79	PSZ2 G255.60-46.18	SPT-CLJ0411-4819			0.42	1.81
87	340.431	−52.163	335.034	−52.490	11.29	5.52	5.00	6.29	8.77	PSZ2 G340.46-52.20		RXC J2220.1-5228	ABELL 3864	0.10	4.57
88	250.275	−17.306	102.809	−40.622	11.14	5.72	4.88	6.26	8.75	PSZ2 G250.29-17.29	SPT-CLJ0651-4037			0.27	6.74
89	252.457	−25.533	92.937	−45.042	10.76	4.05	4.73	6.03	8.60	PSZ2 G252.46-25.53			ACOS 574	0.01	2.43
90	266.550	−27.326	93.971	−57.766	10.67	7.09	4.70	5.97	8.55	PSZ2 G266.54-27.31	SPT-CLJ0615-5746			0.97	2.88
91	260.463	−54.460	49.448	−48.820	10.91	6.07	4.97	5.94	8.53	PSZ2 G260.52-54.50	SPT-CLJ0317-4849		ABELL 3113	0.16	5.92
92	329.599	−54.687	344.995	−56.285	10.89	3.75	5.02	5.87	8.49	PSZ2 G329.53-54.73	SPT-CLJ2259-5617		ABELL 3950	0.15	1.58
93	254.072	−58.458	46.081	−44.021	11.62	5.61	5.81	5.80	8.44	PSZ2 G254.08-58.45	SPT-CLJ0304-4401			0.46	1.70
94	279.498	−44.872	53.238	−64.211	10.19	5.11	4.86	5.34	8.12	PSZ2 G279.51-44.85			ACOS 362	0.08	1.44
95	346.823	−45.341	322.386	−50.819	10.36	4.30	5.03	5.33	8.12	PSZ2 G346.86-45.38		RXC J2129.8-5048	ABELL 3771	0.08	4.88
96	335.934	−41.349	319.209	−59.492	9.94	5.12	4.78	5.16	8.00	PSZ2 G335.93-41.35		RXC J2116.8-5929	ACOS 927	0.06	5.62
97	330.555	−40.546	320.482	−63.588	9.84	4.50	4.69	5.15	8.00	PSZ2 G330.53-40.56	SPT-CLJ2121-6335		ACOS 937	0.22	4.99
98	292.079	−71.965	17.569	−44.764	10.76	4.07	5.63	5.13	7.98	PSZ2 G292.08-71.97	SPT-CLJ0110-4445			0.38	1.95
99	295.629	−51.955	23.372	−64.573	9.78	8.48	4.83	4.95	7.86	PSZ2 G295.63-51.96	SPT-CLJ0133-6434			0.33	
100	258.317	−37.882	75.219	−51.263	9.49	4.00	4.78	4.71	7.70	PSZ2 G258.32-37.88	SPT-CLJ0500-5116		ABELL 3303	0.11	

Table C.1. continued.

Id	G. lon. [°]	G. lat. [°]	RA J2000 [°]	Dec J2000 [°]	$(S/N)_J$	$(S/N)_{SZ}$	q_J	$(S/N)_J$-q_J	Significance	PSZ2	SPT	MCXC	Abell	z	M_{500} [$10^{14}\,M_\odot$]
101	269.739	−64.391	33.219	−47.147	9.45	4.67	4.79	4.66	7.66	PSZ2 G269.82-64.35		RXC J0212.8-4707	ABELL 2988	0.12	1.78
102	272.610	−28.890	91.930	−63.244	9.46	4.23	4.87	4.59	7.62						
103	292.968	−65.767	19.319	−50.858	9.68	6.49	5.18	4.50	7.56	PSZ2 G293.01-65.78			ABELL 2893		
104	260.280	−26.081	94.442	−52.035	9.20	3.58	4.80	4.41	7.49				ABELL 3385		
105	314.240	−55.337	359.720	−60.623	9.02	5.49	4.65	4.37	7.47	PSZ2 G314.26-55.35		RXC J2359.3-6042	ABELL 4067	0.10	2.32
106	251.713	−41.693	69.812	−46.017	8.94	3.99	4.59	4.35	7.46		SPT-CLJ0439-4600			0.34	5.36
107	257.241	−46.829	61.490	−49.279	8.99	4.48	4.87	4.12	7.30		SPT-CLJ0405-4916			0.32	5.13
108	251.438	−37.938	75.214	−45.836	9.53	3.13	5.52	4.01	7.23		SPT-CLJ0500-4551				
109	333.905	−43.600	324.438	−60.119	9.03	7.49	5.11	3.93	7.17	PSZ2 G333.89-43.60	SPT-CLJ2138-6008			0.32	5.00
110	260.626	−28.926	89.924	−52.810	8.56	7.07	4.74	3.82	7.10	PSZ2 G260.63-28.94	SPT-CLJ0559-5249			0.60	5.91
111	324.286	−73.835	5.023	−41.968	8.90	3.50	5.17	3.73	7.03				ABELL 2763		
112	244.117	−53.593	54.249	−39.829	8.40	6.26	4.76	3.65	6.98	PSZ2 G244.11-53.59		RXC J0337.0-3949	ABELL 3142	0.10	1.93
113	269.508	−47.131	56.470	−57.092	8.08	4.14	4.50	3.58	6.93	PSZ2 G269.36-47.20	SPT-CLJ2025-5117	RXC J0346.1-5702	ABELL 3164	0.06	0.75
114	347.588	−35.374	306.490	−51.277	8.19	5.57	4.78	3.41	6.82	PSZ2 G347.58-35.35			ACOS 871	0.22	3.99
115	303.027	−68.574	12.807	−48.554	8.35	3.41	5.05	3.30	6.74	PSZ2 G303.03-68.49	SPT-CLJ0051-4834	RXC J0051.1-4833	ABELL 2830	0.19	3.09
116	341.173	−36.116	308.056	−56.454	8.04	5.92	4.80	3.24	6.70	PSZ2 G341.19-36.12	SPT-CLJ2032-5627	RXC J2032.1-5627	ABELL 3685	0.28	4.80
117	334.025	−49.837	334.988	−57.142	8.37	4.03	5.28	3.09	6.60		SPT-CLJ2219-5708		ABELL 3860	0.33	4.67
118	263.029	−56.198	46.079	−49.352	8.22	4.75	5.13	3.09	6.60	PSZ2 G263.03-56.19	SPT-CLJ0304-4921			0.39	4.28
119	285.899	−74.959	18.675	−41.391	8.34	6.13	5.27	3.08	6.59	PSZ2 G285.87-74.93	SPT-CLJ0114-4123			0.21	2.75
120	356.016	−51.958	330.063	−43.514	9.05	3.08	6.00	3.04	6.57						
121	291.577	−51.264	29.413	−64.380	7.85	3.03	4.84	3.01	6.54				ACOS 210	0.23	3.08
122	248.030	−26.392	90.488	−41.383	7.89	3.87	4.92	2.97	6.51	PSZ2 G247.99-26.37	SPT-CLJ0601-4122			0.27	3.85
123	345.335	−60.017	343.644	−46.335	9.07	5.44	6.13	2.94	6.50	PSZ2 G345.32-59.97	SPT-CLJ2254-4620		ABELL 3937	0.19	2.24
124	260.905	−62.219	39.226	−45.362	7.95	5.40	5.05	2.90	6.47	PSZ2 G260.85-62.19			ABELL 3036	0.33	4.49
125	309.077	−72.506	10.274	−44.498	8.11	3.50	5.24	2.87	6.45		SPT-CLJ0041-4428		ACOS 67	0.41	5.90
126	318.946	−66.813	3.308	−49.110	8.39	3.58	5.52	2.87	6.45		SPT-CLJ0013-4906			0.36	4.13
127	250.693	−27.274	90.059	−43.897	7.61	3.92	4.75	2.87	6.45		SPT-CLJ0600-4353				
128	269.926	−33.562	81.955	−60.928	7.70	4.06	4.84	2.86	6.44						
129	264.378	−35.048	79.615	−56.268	7.65	3.32	4.83	2.82	6.41				ACOS 522	0.32	3.86
130	273.632	−68.444	27.637	−45.174	7.87	5.14	5.07	2.80	6.40	PSZ2 G273.69-68.38	SPT-CLJ0150-4511			0.30	3.72
131	254.686	−34.395	80.582	−48.300	7.73	3.94	4.93	2.80	6.40	PSZ2 G254.66-34.45	SPT-CLJ0522-4818		ABELL 3338	0.05	0.89
132	265.211	−24.979	97.822	−56.170	7.30	3.96	4.59	2.71	6.34	PSZ2 G265.21-24.83		RXC J0631.3-5610			
133	266.726	−34.077	81.239	−58.245	7.58	3.23	4.92	2.65	6.30						
134	259.625	−51.080	54.540	−49.609	7.88	4.22	5.25	2.63	6.28	PSZ2 G259.58-51.07				0.21	3.38
135	295.552	−60.100	19.547	−56.644	7.48	3.14	4.97	2.51	6.20		SPT-CLJ0118-5638		ABELL 2897	0.46	4.53
136	261.307	−36.488	77.318	−53.709	7.42	5.23	4.91	2.51	6.20	PSZ2 G261.28-36.47	SPT-CLJ0509-5342				
137	299.961	−53.485	16.829	−63.551	7.45	3.04	5.15	2.30	6.06						
138	280.717	−52.374	40.161	−59.786	7.34	4.62	5.08	2.26	6.04		SPT-CLJ0240-5946			0.40	4.34
139	256.067	−37.447	75.983	−49.495	7.49	3.87	5.23	2.26	6.03		SPT-CLJ0504-4929		ABELL 3311	0.20	2.69
140	281.296	−46.908	47.813	−63.917	7.07	5.85	4.82	2.26	6.03	PSZ2 G281.26-46.90	SPT-CLJ0311-6354			0.28	3.61
141	268.370	−64.487	33.712	−46.652	7.29	3.30	5.13	2.16	5.97		SPT-CLJ0214-4638			0.27	3.36
142	340.088	−52.584	335.806	−52.480	7.33	3.84	5.24	2.09	5.92		SPT-CLJ2223-5227		ABELL 3872	0.27	3.23
143	250.615	−25.048	93.026	−43.309	6.85	4.22	4.79	2.06	5.90	PSZ2 G250.59-25.03	SPT-CLJ0612-4317		ABELL 3736	0.55	4.91
144	357.745	−41.742	315.890	−43.334	6.73	3.53	4.68	2.05	5.89	PSZ2 G357.75-41.77		RXC J2103.4-4319	ABELL 3283	0.05	1.02
145	254.991	−41.239	70.265	−48.496	6.58	4.66	4.58	2.00	5.86						
146	296.229	−52.033	22.493	−64.590	6.80	6.00	4.82	1.98	5.84	PSZ2 G296.27-52.05	SPT-CLJ0129-6432			0.33	4.06
147	351.816	−54.778	334.758	−45.238	7.26	5.00	5.29	1.97	5.84	PSZ2 G351.76-54.71	SPT-CLJ2218-4519			0.61	5.28
148	252.960	−41.382	70.199	−46.964	6.55	4.43	4.58	1.97	5.84	PSZ2 G252.95-41.35	SPT-CLJ0440-4657			0.35	4.27
149	292.252	−53.065	26.997	−62.875	6.46	3.85	4.54	1.92	5.80				ACOS 194		
150	268.551	−28.149	92.830	−59.627	7.41	4.32	4.71	2.70	5.75	PSZ2 G268.51-28.14	SPT-CLJ0611-5938			0.46	3.94

Table C.1. continued.

Id.	G. lon. [°]	G. lat. [°]	RA J2000 [°]	Dec J2000 [°]	$(S/N)_J$	$(S/N)_{SZ}$	q_J	$(S/N)_J$-q_J	Significance	PSZ2	SPT	MCXC	Abell	z	M_{500} [$10^{14}\,M_\odot$]
151	263.223	-33.187	82.956	-55.344	7.88	6.80	4.78	3.10	5.75	PSZ2 G263.24-33.18				0.30	3.83
152	282.665	-54.841	35.371	-58.601	6.77	3.94	4.77	2.00	5.75					0.13	2.13
153	345.317	-62.251	346.407	-45.204	9.63	3.57	5.26	4.36	5.73			RXC J2305.5-4513	ABELL 3970		
154	265.689	-27.575	93.313	-57.045	7.12	3.48	4.71	2.42	5.67						
155	257.118	-27.233	91.795	-49.483	6.20	3.06	4.59	1.62	5.66			RXC J0607.0-4928	ABELL 3380	0.06	0.87
156	270.400	-44.745	60.078	-58.641	6.93	3.01	5.00	1.93	5.65						
157	330.754	-32.806	302.919	-65.315	5.77	3.69	4.72	1.05	5.65				ACOS 856		
158	250.409	-41.393	70.287	-45.052	5.61	4.04	4.61	0.99	5.62	PSZ2 G250.43-41.42			ABELL 3284	0.15	2.02
159	329.901	-74.561	3.711	-40.593	7.31	5.34	5.53	1.78	5.49		SPT-CLJ0014-4036			0.55	5.67
160	258.554	-22.618	99.187	-49.690	6.48	4.00	4.80	1.68	5.49		SPT-CLJ0636-4942			0.35	3.89
161	254.861	-20.784	100.312	-45.874	6.20	3.74	4.84	1.36	5.47						
162	260.733	-31.256	86.092	-53.151	6.26	4.57	4.73	1.53	5.45	PSZ2 G260.76-31.27				0.25	2.95
163	327.280	-75.170	4.893	-40.415	7.36	4.03	5.54	1.82	5.43						
164	356.230	-43.104	317.814	-44.422	5.59	4.46	4.70	0.90	5.40	PSZ2 G356.21-43.11				0.34	3.35
165	247.682	-25.090	92.055	-40.751	5.88	4.00	4.91	0.96	5.39	PSZ2 G247.69-25.06				0.36	4.12
166	252.248	-50.642	57.037	-45.249	6.62	5.24	5.17	1.45	5.37	PSZ2 G252.23-50.62	SPT-CLJ0348-4515				
167	255.846	-41.583	69.662	-49.106	5.56	3.58	4.53	1.02	5.35						
168	347.751	-59.916	342.696	-45.317	8.50	3.28	6.32	2.17	5.33			RXC J2250.8-4521	ACOS 1067	0.05	0.82
169	252.121	-34.155	80.699	-46.168	6.04	3.08	4.92	1.11	5.33				ACOS 526		
170	295.198	-57.013	21.188	-59.613	6.00	5.23	4.74	1.26	5.33	PSZ2 G295.19-56.99	SPT-CLJ0124-5937		ACOS 157	0.22	3.03
171	319.166	-55.033	354.344	-59.699	6.02	4.51	4.94	1.07	5.29		SPT-CLJ2337-5942			0.77	5.75
172	246.470	-38.671	73.948	-41.976	7.03	3.00	5.45	1.57	5.26		SPT-CLJ0455-4159			0.31	3.38
173	346.731	-57.456	339.853	-46.882	9.40	3.52	6.77	2.63	5.26						
174	258.418	-38.557	74.136	-51.305	5.89	4.48	4.78	1.11	5.26	PSZ2 G258.33-38.54	SPT-CLJ0456-5116			0.56	4.58
175	290.504	-71.045	18.586	-45.527	7.07	3.02	5.64	1.43	5.25						
176	248.782	-29.959	85.981	-42.789	5.66	3.68	4.89	0.76	5.22		SPT-CLJ0543-4250			0.59	4.49
177	277.000	-51.584	44.412	-58.716	6.48	3.58	5.28	1.20	5.22		SPT-CLJ0257-5842			0.44	4.51
178	245.510	-29.222	86.190	-39.854	6.27	3.18	5.18	1.09	5.22		SPT-CLJ0544-3950			0.45	4.25
179	249.394	-34.217	80.293	-43.930	5.58	3.56	4.84	0.74	5.19						
180	262.045	-32.976	83.288	-54.353	5.84	4.60	4.85	0.99	5.18	PSZ2 G262.01-32.98				0.23	2.72
181	269.014	-55.228	44.560	-52.727	5.62	3.09	4.82	0.80	5.14				ABELL 3074		
182	357.238	-34.672	306.147	-43.350	5.79	3.51	4.87	0.91	5.14						
183	323.083	-63.990	358.996	-50.913	5.07	5.08	4.37	0.71	5.11	PSZ2 G323.08-63.98	SPT-CLJ2355-5055			0.32	4.22
184	345.215	-32.903	302.377	-53.179	5.87	3.47	5.02	0.84	5.04				ABELL 3665	0.24	
185	251.548	-42.792	68.244	-45.837	5.09	4.28	4.55	0.54	5.03	PSZ2 G251.55-42.78			ABELL 3270	0.53	4.87
186	318.019	-58.895	358.740	-56.548	5.06	4.58	4.57	0.50	5.02	PSZ2 G318.05-58.88	SPT-CLJ2354-5633			0.34	3.34
187	268.411	-43.638	63.012	-57.710	5.46	3.37	4.85	0.61	4.99	PSZ2 G268.34-43.64	SPT-CLJ0412-5743				
188	267.374	-46.219	59.056	-56.124	5.42	4.14	4.79	0.63	4.99	PSZ2 G267.30-46.19					
189	279.016	-56.371	36.612		6.64	3.19	5.71	0.92	4.99						
190	268.091	-59.722	39.274	-49.647	5.73	3.42	5.15	0.58	4.95		SPT-CLJ0236-4938		ABELL 3019	0.33	3.43
191	333.125	-35.446	308.253	-63.019	6.05	3.70	5.16	0.89	4.95				ABELL 3687	0.08	
192	283.847	-65.365	25.079	-49.914	6.65	3.52	5.86	0.79	4.93						
193	305.262	-71.942	11.835	-45.167	6.35	3.12	5.54	0.81	4.92		SPT-CLJ0047-4506		ACOS 1022	0.39	4.56
194	324.836	-46.138	336.297	-64.282	4.98	3.13	4.56	0.42	4.91				ABELL 3688	0.09	
195	0.622	-48.152	324.445	-41.074	6.72	3.11	5.98	0.74	4.89						
196	1.499	-35.778	308.172	-40.026	5.86	3.71	5.28	0.57	4.87						
197	272.628	-24.433	101.650	-62.645	5.47	3.83	4.91	0.57	4.86		SPT-CLJ0646-6236			1.20	4.66
198	352.487	-33.184	303.471	-47.119	5.69	3.73	5.14	0.55	4.86						
199	335.748	-37.097	310.996	-60.647	5.56	3.36	5.03	0.53	4.84						
200	260.921	-35.301	79.333	-53.436	5.54	3.03	4.98	0.57	4.84						

Table C.1. continued.

Id.	G. lon. [°]	G. lat. [°]	RA J2000 [°]	Dec J2000 [°]	$(S/N)_J$	$(S/N)_{SZ}$	q_J	$(S/N)_J$-q_J	Significance	PSZ2	SPT	MCXC	Abell	z	M_{500} [$10^{14} M_\odot$]
201	255.932	-52.549	53.538	-46.977	5.76	3.70	5.20	0.56	4.84		SPT-CLJ0334-4659			0.49	4.23
202	305.616	-54.819	9.538	-62.240	5.33	4.11	4.94	0.39	4.77	PSZ2 G305.59-54.80					
203	292.378	-57.126	24.015	-59.079	5.20	3.69	4.84	0.35	4.76	PSZ2 G292.40-57.11	SPT-CLJ0135-5904			0.49	4.57
204	265.024	-30.437	87.988	-56.765	5.11	3.45	4.74	0.37	4.74						
205	284.523	-47.939	42.558	-64.722	5.35	4.02	4.99	0.36	4.71				ABELL 3061		
206	356.548	-41.337	315.336	-44.232	4.89	3.84	4.69	0.20	4.70						
207	310.626	-63.554	7.143	-53.231	4.46	4.46	4.32	0.14	4.69				ABELL 2779		
208	277.913	-65.311	28.381	-48.691	5.34	3.97	5.06	0.28	4.68						
209	274.955	-58.096	37.411	-53.368	5.72	3.12	5.43	0.29	4.65						
210	327.637	-54.292	345.963	-57.369	5.51	4.67	5.22	0.29	4.65	PSZ2 G327.66-54.26				0.58	5.05
211	274.185	-53.288	44.073	-56.304	5.89	4.36	5.57	0.32	4.64		SPT-CLJ0256-5617				
212	282.535	-53.687	36.837	-59.477	5.34	3.13	5.16	0.18	4.62						
213	258.667	-34.133	81.229	-51.574	4.98	3.45	4.85	0.13	4.58						
214	253.736	-47.436	61.300	-46.822	4.96	3.54	4.82	0.13	4.57		SPT-CLJ0405-4648			0.39	3.88
215	261.447	-30.962	86.667	-53.736	4.91	3.12	4.79	0.12	4.56		SPT-CLJ0546-5345			1.07	4.00
216	245.673	-50.813	57.723	-41.115	5.06	3.44	4.99	0.08	4.55		SPT-CLJ0351-4109			0.68	5.16
217	326.406	-68.015	0.288	-46.755	5.89	3.02	5.66	0.23	4.55				ABELL 4075		
218	274.682	-64.879	30.412	-48.217	5.25	3.51	5.13	0.12	4.54				ACOS 218	0.09	
219	260.348	-20.324	103.375	-50.613	4.94	4.43	4.87	0.07	4.53						
220	252.269	-23.928	95.065	-44.475	4.96	3.64	4.88	0.08	4.53						
221	319.266	-48.599	346.674	-65.073	5.14	4.48	5.06	0.08	4.52	PSZ2 G319.19-48.59	SPT-CLJ2306-6505			0.53	4.34
222	264.135	-35.097	79.543	-56.066	4.63	3.41	4.61	0.03	4.51						
223	254.233	-25.041	94.169	-46.485	4.84	3.19	4.82	0.01	4.51						
224	325.000	-49.228	341.209	-62.122	5.38	4.60	5.36	0.01	4.48	PSZ2 G324.99-49.26	SPT-CLJ2245-6206			0.58	4.70
225	328.390	-59.170	351.147	-53.453	5.77	3.46	5.65	0.13	4.43						